Theses and Dissertations

Spring 2019

Finite Element Electromagnetic (EM) Analyses of Induction Heating of Thermoplastic Composites

Ankit Patel

FINITE ELEMENT ELECTROMAGNETIC (EM) ANALYSES OF INDUCTION HEATING OF THERMOPLASTIC COMPOSITES

by

Ankit Patel

Bachelor of Engineering
Gujarat Technological University, 2014

_____

Submitted in Partial Fulfillment of the Requirements

For the Degree of Master of Science in

Electrical Engineering

College of Engineering and Computing

University of South Carolina

2019

Accepted by:

Mohammod Ali, Director of Thesis

Michael Van Tooren, Reader

Guoan Wang, Reader

Cheryl L. Addy, Vice Provost and Dean of the Graduate School

www.manaraa.com

ACKNOWLEDGEMENTS

ABSTRACT

Thermoplastic composites are in great demand for current and future manufacturing of aircraft and automotive industries. Induction heating and welding of thermoplastic composite laminates is of great significance. The non-contact method of heating and welding is being adopted in aircraft parts, engine parts, and turbine parts manufacturing among many other things. This thesis performs simulations and analyses of Electromagnetic (EM) induction heating of thermoplastic composites materials.

The induction heating and welding of thermoplastic composites in the presence of a susceptor alloy (called Monel) consisting of 67% nickel and 27% copper is studied using a Finite Element Analysis (FEA) software. A primary current carrying coil was excited using 500A of current at 292 kHz frequency, which exposed the Monel susceptor underneath it. The EM fields created by the primary coil caused induced current in the Monel mesh, which caused losses. Temperature rise in the material is synonymous to the losses in the material. The I^2R losses in the Monel material was used as the basis to calculate the temperature rise in the material. Simulation results clearly show the heating patterns on the Monel mesh, less in the center and high on the edges. Location-based temperature increases due to I^2R losses are calculated which show significant heating and welding potentials. The result obtained from the simulation was validated using an experiment. Measured temperature increase showed the reading of 40 and 43.9 degrees

respectively (thermocouple and IR camera). These numbers compare favorably with the simulated temperature increase of 38.97 degrees C.

Also, the induction heating of Carbon fiber reinforced composites (CFRC) were simulated and studied. The results obtained from the simulation explain that fiber orientation and the presence of resin are two critical parameters that affect the output e.g. the solid loss. Due to the challenges in the high aspect ratio of the models, i.e. very small fiber diameters and many fibers within a very small dimension only smaller sized models were simulated. Furthermore, instead of a circular cross-section a polyhedron cross-section for the fiber model was considered to successfully complete the simulations. It was found that simulation models containing fibers oriented in 0 and 90 orientation yielded higher solid loss than fibers oriented in the same direction. It was observed that for fibers with resin present in between them yielded far greater solid loss compared to no-resin cases, especially for very small separation distances between fibers. Especially, for the 0, 90 orientation of fibers and in the presence of resins solid loss was nearly 200 times that for fibers with 0,0 orientation and that were at short distance from one another.

TABLE OF CONTENTS

LIST OF TABLES

LIST OF FIGURES

CHAPTER 1
INTRODUCTION

1.1 Motivation for Work

With the recent drive towards the use of composite materials for aircrafts that takes advantage of their high strength and low weight in lieu of metals, welding two parts of the thermoplastic composites have gained much attention [1]. While there are many methods of welding that can join two pieces of thermoplastic composites non-intrusive induction heating based welding has become very attractive [1]. This technique is also known as contactless welding technique because there is no contact between the parts to be welded and the primary high current carrying conductive coil. Thermoplastic composite (TPC) parts are welded using induction heating in the presence of a susceptor. Composites materials are used in building aircraft parts, turbines, engines, and many more applications. Weight reduction is the greatest advantage of composite material usage and is the key factor in using it in aircraft structures. Composite materials are stronger than traditional aluminum found on most aircrafts, and they provide a smooth surface and increase fuel efficiency, which is a huge benefit [1].

Moreover, large aircraft companies like Boeing are planning to replace all of their metals parts with composite materials in the coming future. They even want to replace the bolts and nuts that joining two parts. Hence, the behavior of composite material needs to

1

be understood in detail. Besides, the temperature distribution over the composite while welding and the quality of weld are paramount. This area is fascinating for research.

The focus of this M.S. thesis is an attempt to study the induction heating of composite materials using a current carrying conductor. Starting from an analytical formulation this thesis investigates the power losses in the material due to the current in a coil. Simulation studies are conducted for thermoplastic composite welding in the presence of a susceptor material using Ansys Maxwell. Simulation models were also created to investigate and understand the heating due to induction mechanism for carbon fibers both in the presence and in absence of resins. Multi-layer fibers in 0, 90 and other orientations are considered.

1.2 Overview of Thesis

The first chapter goes over the objectives and motivation behind the work presented and gives an outline of the thesis and the scope of each chapter. A literature study was carried out to determine what others have done in this field of research, and different welding technique used in the past are discussed in the second chapter. The third chapter looks at the induction welding of thermoplastic composites in the presence of a susceptor, Monel. The primary goal was to determine the heat distribution on a Monel mesh and compare the simulation results with experimental results. Temperature was calculated from the current density using equations. The next chapter discusses analytical calculation of near-field currents for inductive thermoplastic welding. In this chapter, many equations were derived to compare the analytical results with simulation results. In chapter five, induction heating of carbon fiber composites is explained. Fiber orientation and the amount

of resin present are the variables on which output results mainly depend on. Interface heating hypothesis is also explained in detail. It was assumed that the heating is mainly occurring at the interface where the fiber direction is perpendicular to each other. The conclusion and the future scope of this work are explained in chapter six.

CHAPTER 2
LITERATURE OF THERMOPLASTIC WELDING

2.1 Introduction

The use of composite materials has proliferated significantly in the past two decades and is continuing. Composites are classified into two different groups, such as thermoplastic composites and thermoset composites. Thermoplastic and thermoset are two separate classes of composites polymers, which are differentiated based on their response in the presence of heat. Both of these groups have different properties and applications. The main difference between these two polymer groups is that thermoplastic polymers attain malleable properties above a specific temperature and solidifies upon cooling. On the other hand, thermoset polymers cannot withstand high temperature.

Thermoplastics are preferred over thermoset composites. Thermoplastic composites are widely used in various applications in the modern world. Thermoplastics are generally of high molecular weight where the polymer chains are associated together via intermolecular forces. These forces can be easily broken when energy is supplied. This is the reason why the polymer is moldable and melts upon heating. When enough energy is supplied to get rid of the intermolecular forces that hold the polymer as a solid, solid melting takes place. When it is being cooled, the polymer gives off heat and re-forms the intermolecular forces making it solid. Therefore, the process is reversible. Once the polymer is melted, it can be molded into different shapes and upon re-cooling different

4

products can be obtained [2]. Thermoplastics are perfect for manufacturers because of their recyclable nature. Thermoplastics can be found throughout the entire body of a vehicle, both inside and outside. It weighs 60% less than aluminum; therefore, it increases the efficiency of vehicles. Welding is required to join two parts of thermoplastics. The quality of the weld is important, and it mainly depends on the weldability of the material and the method used for welding. Hence, different thermoplastic materials and various welding methods are discussed in this chapter.

2.2 Thermoplastic Materials

Thermoplastic is a plastic material that becomes soft when heated and hard when cooled. Thermoplastic materials can be cooled and heated several times without any changes in their properties [3]. They can be heated and molded into different shapes according to the applications, several times.

Some benefits of thermoplastic include their lightweight, high strength, better fatigue properties than metals, high recyclability, high impact resistance, reshaping capabilities, hardness and crystallinity, and eco-friendly manufacturing. Some disadvantages include high cost and low melting point.

2.3 Types of Thermoplastics Materials

There are many different types of thermoplastic materials, with all having their applications. The most commonly welded thermoplastics materials are listed below with their applications.

1) **PMMA (Polymethyl Methacrylate)** is also known as Plexiglas. It is mainly used as a substitute for glass items such as aircraft windows, lenses of exterior lights of automobiles, aquarium, and motorcycle helmet visors. In the medical field, it is used in bone cements and to replace eye lenses [3].

2) **PPS (Polyphenylene Sulfide)** has excellent flame retardance, excellent electrical properties, and a low coefficient of friction. It is principally used in coating applications. PPS can be used in injection and compression molding at a temperature (300 to 400 C) at which PPS particles soften and undergo crosslinking. Its applications are in cookware, bearings, etc. [3].

3) **PP (Polypropylene)** is useful for such diverse products as reusable plastic food containers, ropes, plastic moldings, car batteries, insulation for electrical cables and piping system. In medicine, it is used to make heat-resistant medical equipment [3].

4) **PE (Polyethylene)** is resistant to moisture and most chemicals. It is flexible at room temperature and can be heat-sealed. It is one of the inexpensive plastics hence its use in many different applications such as; moving machine parts, bulletproof vests, portable gasoline cans, gas pipes, transporting and handling boxes of durable goods, and standard household food covering [3].

5) **PVC (Polyvinyl chloride)** is a tough, lightweight material that is resistant to acids and bases. It is mainly used in the construction industry, such as drainpipes, gutters, and roofing sheets. It is also converted to flexible forms with the addition of plasticizers; thereby it is useful for hoses, tubing, electrical insulation, coats, and jackets. PVC bends easily while

transits, therefore to repair the plastic is heated until it becomes malleable, then re-bend the material in a correct form [3].

6) CFRP (Carbon fiber Reinforce Polymers) when compared to thermoset fiber, reinforced carbon fiber laminates are more comfortable to process as they do not require complex chemical reaction not lengthy curing process, they are easily recyclable and do not need refrigeration for storage. This thermoplastics material are useful for current and future aircraft components.

2.4 Thermoplastic Welding

Thermoplastic welding is a process used to join two pieces of thermoplastic materials using heating, pressure, and cooling. First, the surfaces of the thermoplastic materials are heated to their melting points; different materials have different melting points, typically ranging between 250 to 500 degrees Celsius. Second, the materials are pressed together until they cool. Pressure is applied so that molecules in one material can bond with the molecules of the other material. Numerous welding methods have been developed for joining thermoplastics materials. These methods are classified as external and internal heating methods, based on the heating mechanism on the welding interface. Further classification is as shown in the figure below.

An external method is also known as a thermal method. Moreover, there are six different welding techniques under the thermal method. Whereas internal methods are, divided into two parts, mechanical and electromagnetic. One of the most used welding techniques from each group is explained in detail.

7
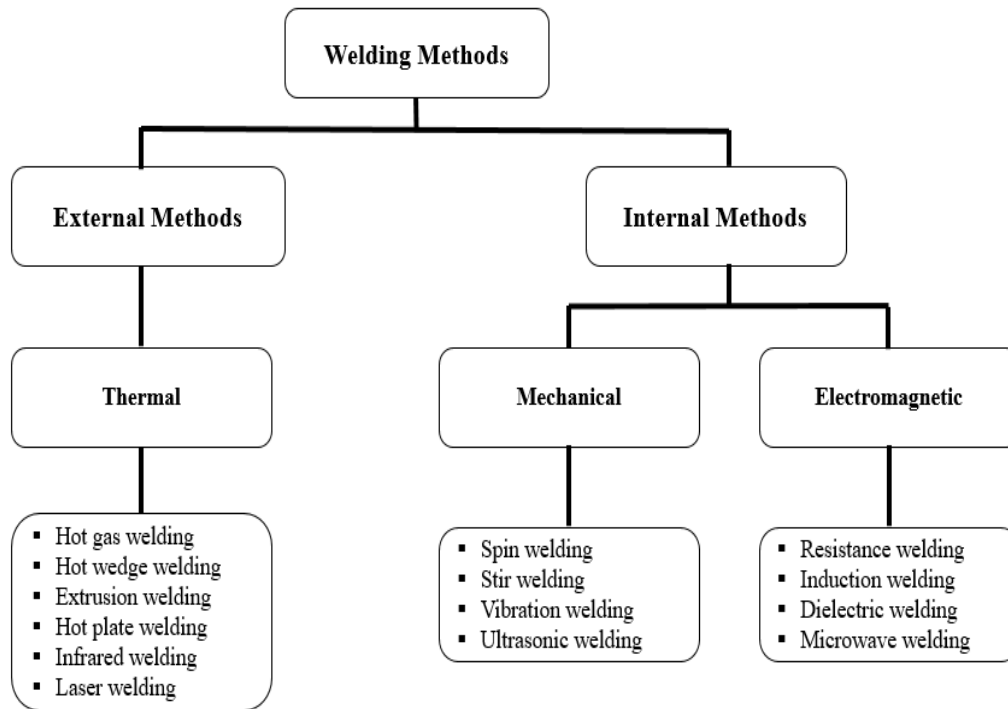
Figure 2.1: Classification of welding techniques for thermoplastic composites.

2.4.1 Thermal Welding Methods

Thermal welding is a fusion bonding methodology that consists in heating polymer matrix composites pieces at their interface causing a decrease of viscosity thus allowing polymers chains to interfuse as the surfaces are held tightly together, with further slow cooling for joint consolidation [4-6].

2.4.1.1 Hot Plate Welding

Hot plate welding is one of the most popular methods for joining thermoplastics out of six techniques in thermal welding. The reason behind this is that this method is a simple, reliable and cheap way of producing firm welds. There is a three-step process: heating, joining and cooling.

8
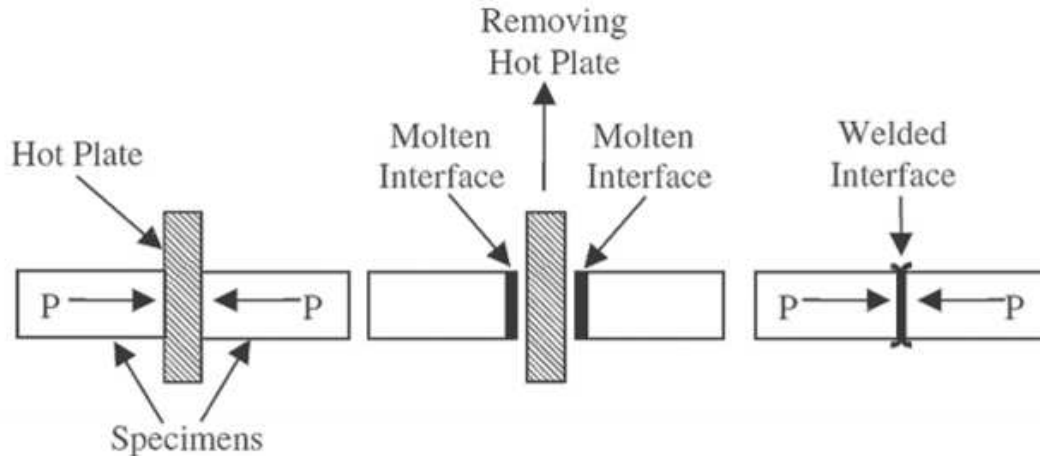
Figure 2.2: Schematic of the hot plate welding [6].

Figure 2.2 explains the process of hot plate welding. The two parts to be welded are called specimens and there is a hot plate in between the two specimens. Adequate pressure must be applied to enforce the hot tool against the specimens. This applied pressure is important because if the pressure is less than required it will result in cold welding. In addition, if the applied pressure is excessive, the melt will be pressed into flash and insufficient amount of material will remain on the surface. Once the surface of the specimens is molted the hot plate is removed and the two molten interfaces are pressed together to form a welded interface.

An external heating element (polytetrafluoroethylene-coated hot metal plate) is placed between the two parts to be welded. The ends of two parts to be welded will melt when kept in contact with the hot metal plate for some time. Pressure on two thermoplastic parts is maintained so that the thermoplastic matrix begins to soften and melt. After this, the hot metal plate is removed, and the two melted ends of thermoplastic are pressed against each other until consolidation occurs. Consolidation for small parts can be completed in less than one minutes. However, it requires at least half an hour for large parts to get a good

weld. The disadvantage of this technique is that the surface of the thermoplastic is contaminated.

2.4.2 Electromagnetical Welding Method

There are four different techniques for to perform welding under the electromagnetic welding method. The most used technique in this category is the Induction welding method followed by the resistance welding method. Both of these techniques are explained in detail.

2.4.2.1 Induction Welding

Induction heating and welding is a unique technique used in order to weld two similar or dissimilar parts of thermoplastic composites. This method is different because there is no contact between the parts to be welded and the primary coil. Thus, it is a contactless welding method. Heating can generally be controlled, within a specific area. The components to be welded are exposed to an alternating electromagnetic field. When there are electrically conductive loops in the component, e.g., due to carbon fiber reinforcement, an eddy current is induced, resulting in efficient, localized heating of the laminate [7].

There are three categories of heating sources during induction welding of fiber reinforced thermoplastic composites: fiber heating, dielectric heating, and contact resistance heating.
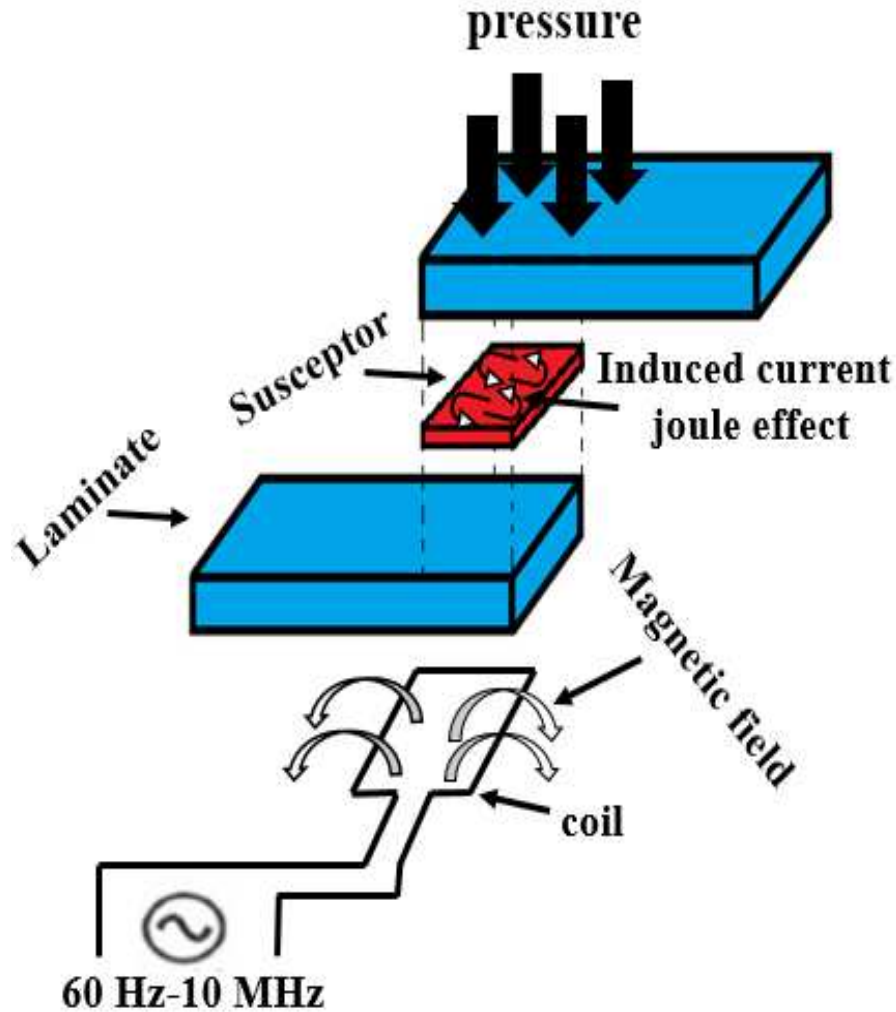
Figure 2.3: Schematic illustration of a magnetic field and eddy current generated by an electromagnetic coil.

1) Fiber heating is the result of Joule losses due to the inherent resistance of the fibers. This loss is dependent on fiber diameter, fiber length, and resistivity.

2) A very thin layer of dielectric material separates preconsolidated laminates. When an alternating electric field is applied to the laminate, a potential difference is created between the fibers whether in (0,0) or (0,90) orientations. For very small separation distance between fibers, the electric field magnitude can be very high.

11
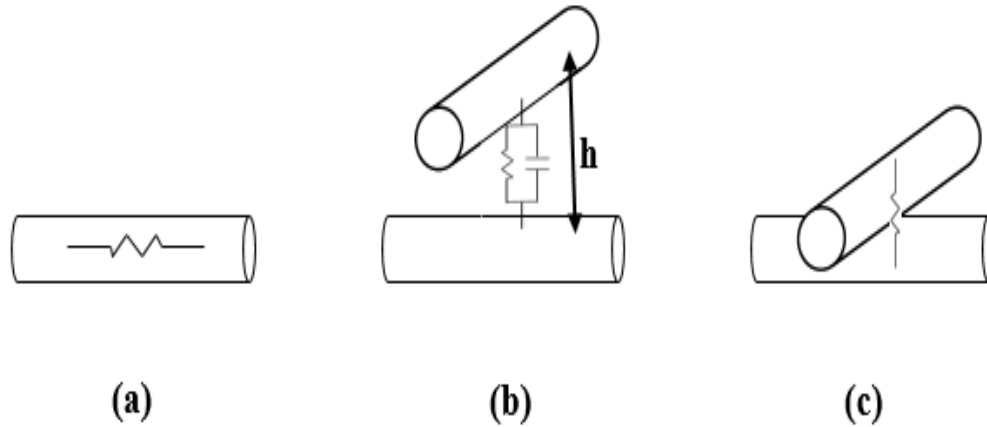
Figure 2.4: Induction heating mechanisms (a) fiber heating, (b) dielectric heating, (c) contact resistance.

3) The third heating mechanism is fiber-to-fiber contact. When the fibers in the plies are arranged in angles, this mechanism becomes dominant. Because of the contact, there is a significant temperature and pressure dependent resistance at fiber junctions, which generates heat [7].

Grumman Aircraft Laboratories [8] report induction heating as highly suitable for both the construction and repair of carbon fiber reinforced thermoplastic parts of the F-111A aircraft stabilizer leading edge demonstration component, using graphite fibers as the conducting element. Structural elements produced by this method compared favorably to those manufacturers by autoclave co-consolidation. The examples above show that induction heating can be used for welding of thermoplastics fibers reinforced composites and acceptable bonding properties are obtained.

2.4.2.2 Resistance Welding

Resistance welding has been considered a very promising joining technique for aerospace application. This process is relatively fast (welding time from 1 to 4 minutes),

12

requires a little amount of material and can be applied to large structures. Good thermal insulation and a correct amount of input energy can reduce the welding time and enhance the weld quality [9-12]. In this process, a conductive element (generally a steel mesh or a carbon strip) is placed at the interface between the laminates to be joined. This conductive element is connected to a power supply, and then a sufficient I is applied so that Joule loss generated enough heat to create a bond line [9-12]. Figure 2.5 shows a schematic of the resistance welding process.
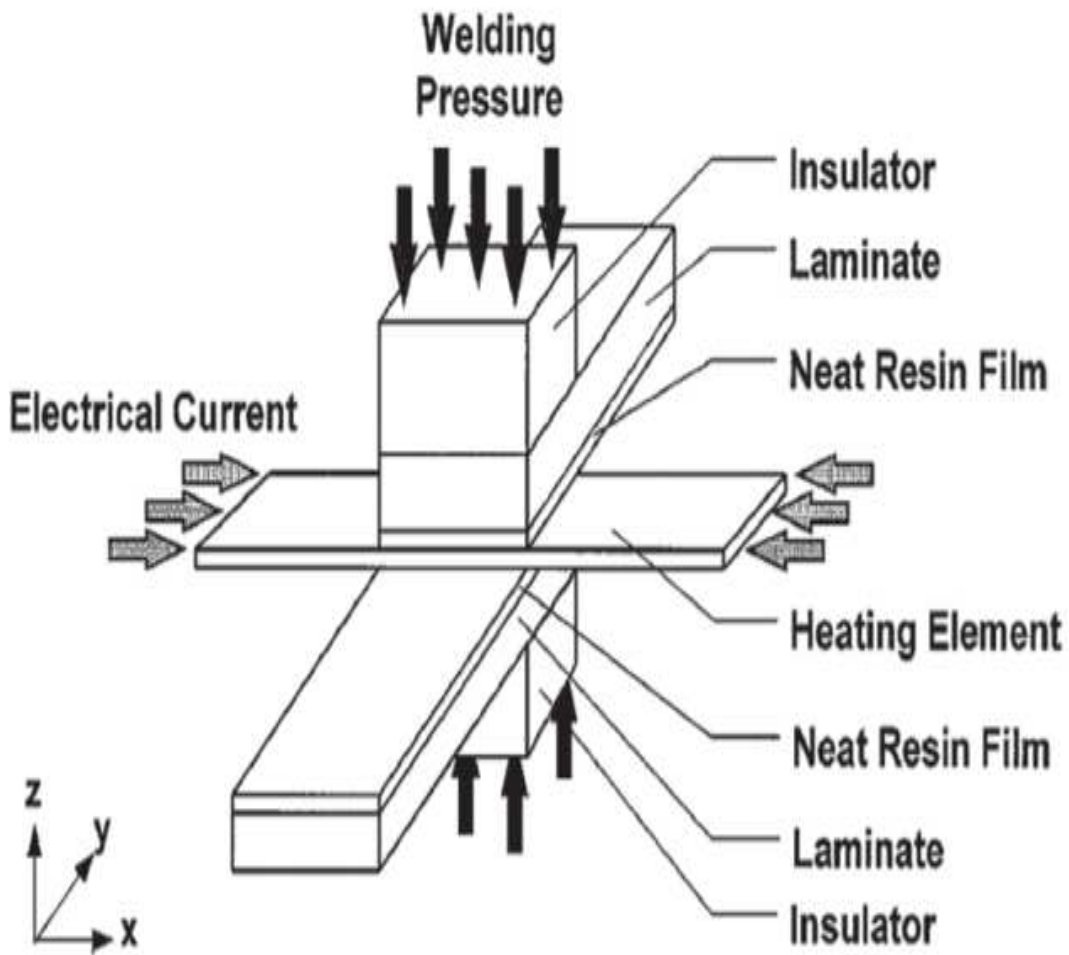
Figure 2.5: Schematic set-up for resistance welding process [4].

13

The electrical connection between the heating element and the power circuit is critical to the resistance welding process. In order to introduce adequate current into the heating element, several ways have been used, including direct clamping on the prepreg; clamping on the bare fibers; prepreg dipped into the liquid metal bath; clamping on the bare fibers painted with silver filled epoxy compound, among others. Instead of using continuous power during the process, power can be applied in the form of intense pulses. This process is called impulsive resistance welding and requires less energy to melt the matrix due to lower heat losses [13].

This welding process can also be carried out under either constant load or displacement control. The method can produce lap shear strength values greater than 33 MPa and has been used in order to weld PEEK and PEI laminates by the US Air Force [14].

2.4.3 Mechanical Welding Method

There are four welding methods in this category. Spin welding, vibration welding, ultrasonic welding, and stir welding. Ultrasonic welding is the most used technique out of the four. This technique is explained in detail.

2.4.3.1 Ultrasonic Welding

Ultrasonic welding is a process in which high frequencies are used (typical frequencies range from 15 to 70 kHz) in order to induce molecular motion, thus creating friction, which is converted to heat. The ability to weld two or more components using ultrasonic welding depends on material physical properties, frequency, and amplitude of ultrasonic wave and joint design. Figure 2.6 represents a schematic of an ultrasonic welding

14

machine using a piezoelectric transducer, by which the oscillations are generated by applying electrical power at a high-frequency. All ultrasonic welding systems are composed of the same essential elements:

(a) A press to put the two or more parts to be assembled under P

(b) A nest or anvil in which the parts are placed allowing the high frequency vibration to be applied

(c) An ultrasonic stack composed of a transducer

(d) A converter, to convert the electrical signal into mechanical vibration

(e) Booster to modify the amplitude of the ultrasonic vibration

(f) A sonotrode to apply the mechanical vibration to the parts to be welded

(g) An ultrasonic generator to provide and control the ultrasonic energy [4, 8, 15-17].

The application of ultrasonic welding is quite extensive in many industrial branches including electrical, computer, automotive, aerospace, energy, medical and packaging. In particular, the aerospace industry employs this methodology to join lightweight thermoplastics matrix composite materials, and many studies have been conducted to find optimum parameters and process windows to produce high-quality welds [15-17].
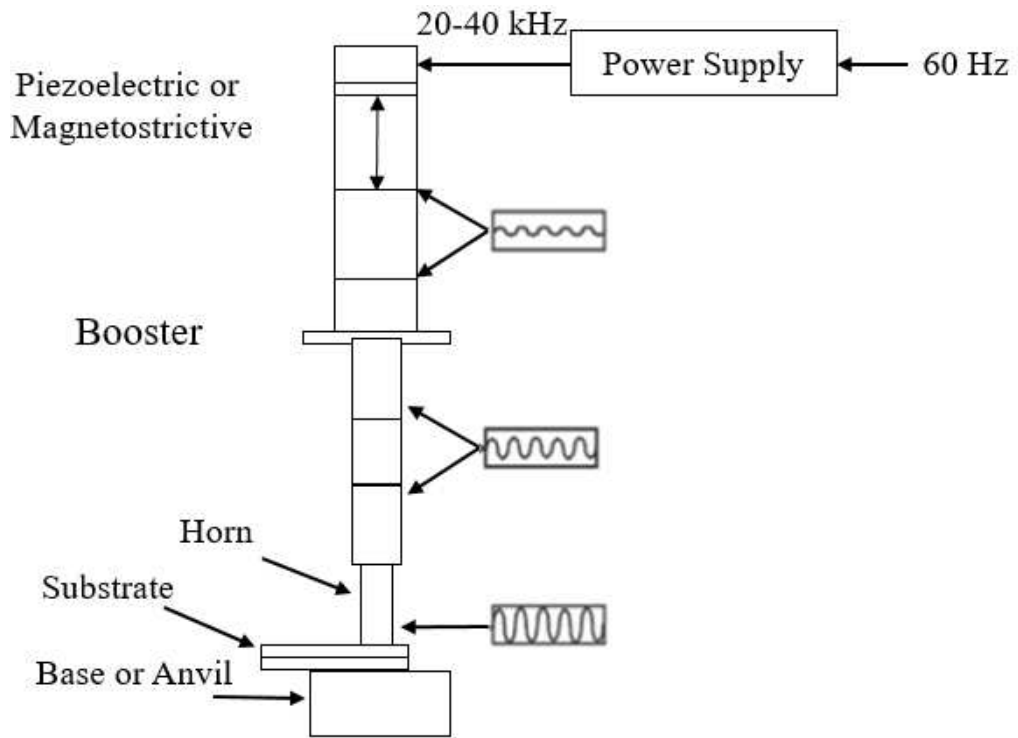
Figure 2.6 Schematic of an ultrasonic welding machine.

CHAPTER 3

INDUCTION HEATING IN THE PRESENCE OF MONEL

3.1 Introduction

This Chapter discusses susceptor based induction welding of two Thermoplastic Composite (TPC) parts where the Monel material is used as the susceptor. The quality of a weld depends on sufficient and homogenous heat generation on the Monel susceptor. Therefore, the focus here is to study the heating mechanism of Monel as function of various parameters. The study was conducted using Ansys Maxwell details about which are explained later. Experimental results are also presented and compared with results obtained from simulation.

Induction heating is a unique technique used in order to weld two similar or dissimilar parts of thermoplastic composites. This method is different because there is no contact between the parts to be welded and the primary coil. Thus, it is a contactless welding method. Heating can generally be controlled, within a specific area. Typically, the source coil travels over the area to be welded. Hence, at one instant the electromagnetic field exposes a specific area over a period. The exposure time is a variable and must be optimized.

17
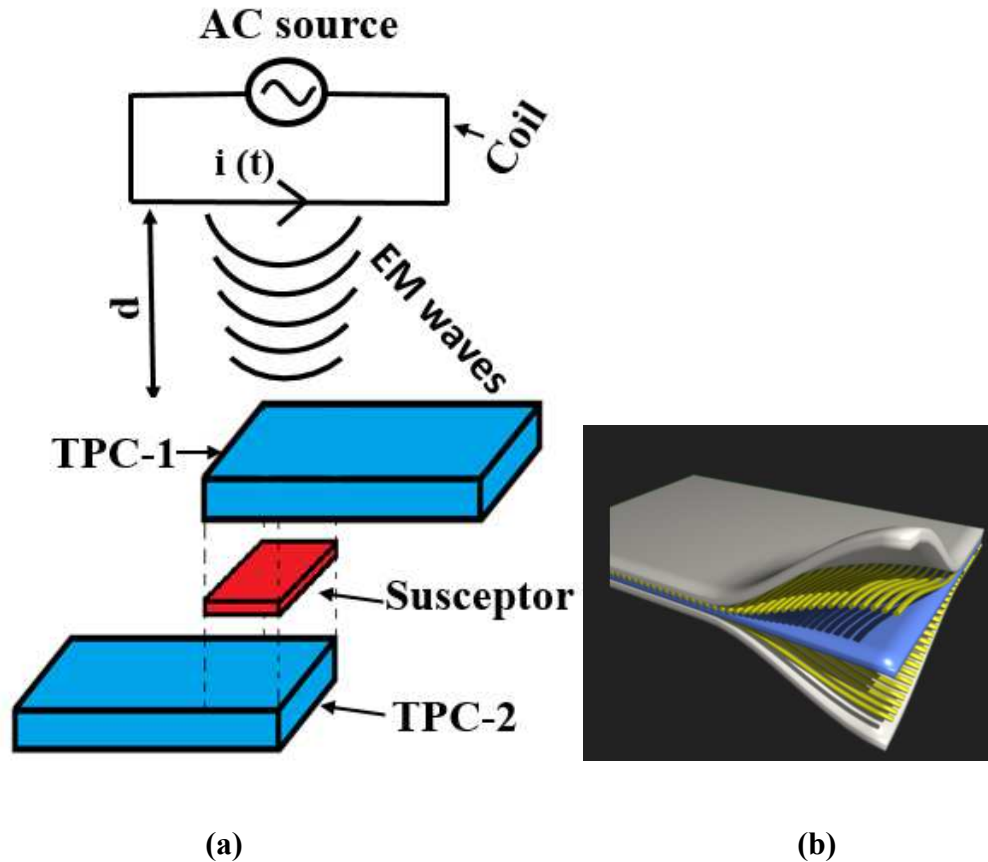
Figure 3.1: Induction welding (a) basic setup, (b) TPC with many layers [By Per OX [Public domain], from Wikimedia Commons].

In Figure 3.1 (a), shows basic setup for welding two TPC parts using induction heating. The distance between the bottom of the coil and the top of TPC-1 is d. The two blocks to be welded are TPC-1 and TPC-2. The susceptor (Monel) is sandwiched in between the two blocks. TPCs concerned here are woven glass fibers which are infused with resin. Many layers of woven glass fibers are compacted together and then is infused with resin to create a block of TPC. Figure 3.1 (b) Shows TPC composite panels or sheet which have been fabricated as described.

- Working Principle: An alternating current powers the inductive coil with a fixed frequency. As the current flows in the coil, it produces an alternating

electromagnetic (EM) field in and around the coil. The EM field causes losses and resulting heat in the thermoplastic composites and Monel. The Monel material serves as a susceptor with large amount of resistive loss due to its higher magnetic permeability which heats up the thermoplastics and bond them together. Monel is melted to weld the two TPC's. Once the entire specimen cools down naturally, the welding process is complete.

3.2 Monel

Robert Crooks Stanley, who worked for the International Nickel Company (INCO) in 1901, invented Monel. Monel alloy 400 is a binary alloy of the same proportions of nickel and copper as is found naturally in the nickel ore from the Sudbury (Ontario) mines and is therefore considered a puritan alloy [18-19]. A 'puritan' alloy is one whose main constituents are supplied from a base ore with the same composition, thus not requiring to be blended with material from another ore. Monel was named after company president Ambrose Monell and patented in 1906 [20]. One L was dropped because family names were not allowed as trademarks at that time [21].

Monel is a trademark of Special Metals Corporation under which a series of nickel-copper alloys are grouped. Commercially there are many types of Monel's available, such as alloy 400, alloy 401, alloy R-450, alloy K-500 and Monel 404 [22].

Monel is a group of nickel alloys, primarily composed of nickel (up to 67%) and copper (around 30%), with small amounts of iron, manganese, carbon, and silicon [23]. Most of the simulation models were created using Monel 400 alloy. Moreover, experiments were also performed using Monel 400 alloy. Monel is stronger than pure nickel, and are

resistant to corrosion by many agents, including rapidly flowing seawater [23]. It is a very expensive alloy, with the cost ranging from 5 to 10 times the cost of copper and nickel, hence its use is limited to those applications where it cannot be replaced with cheaper alternatives. Compared to carbon steel, piping in Monel is more than three times as expensive [24].

3.2.1 Composition of Monel Alloy

Table 3.1 below shows the amount of different materials used to make different Monel alloys [25]. As shown in Table 3.1, the primary material used to make Monel is nickel and the second most important material is copper. In each group of alloys, there are many different mesh sizes available. For Monel 400, there are three different mesh sizes, which are 100X100 mesh per square inch, 40X40 mesh per square inch, and 20X20 mesh per square inch.

3.3 Ansys Maxwell Simulation Model Development

Ansys Maxwell is a high-performance low frequency software that uses Finite Element Analysis (FEA) to solve electromagnetic (EM) problems. Maxwell solves EM problems by solving Maxwell equation's in a finite region with assigned boundary conditions and initial conditions set by the user. For all the models an AC source with 500 A current at 292 KHz frequency was used.

20

Table 3.1: Constitutive parameters of various Monel alloys.

Trade Name	Alloy Type	UNS	%Cu	%Al	%Ti	%Fe	%Mn	%Si	%Ni
Monel 400	B 127, B 164	N04400	28-34			2.5 max	2.0 max	0.5 max	63 min
Monel 401		N04401	28-34			2.5 max	2.0 max		63 min
Monel 404		N04404	Rem	0.05 max		0.5 max	0.1 max	0.1 max	52-57
Monel K-500	B 865	N05500	27-33	2.3-3.15	0.35-.85	2.0 max	1.5 max	0.5 max	63 min
Monel 405	B 164	N04405	28-34			2.5 max	2.0 max	0.5 max	63 min

As shown in Figure 3.2, there are different layers in creating the model using the software; first, the Monel mesh is created, second, the thermoplastic composite blocks are created, and finally the coil on top is created at a d=3mm. The thickness of each TPC considered is 3 mm. The coil is made of copper as a conductor, the mesh is made of Monel,

and TPC's are made of Plexiglass. Plexiglass is used because it has similar substrate properties ($\varepsilon_r = 3.4$ and $\tan \delta = 0.001$) as thermoplastics composites.
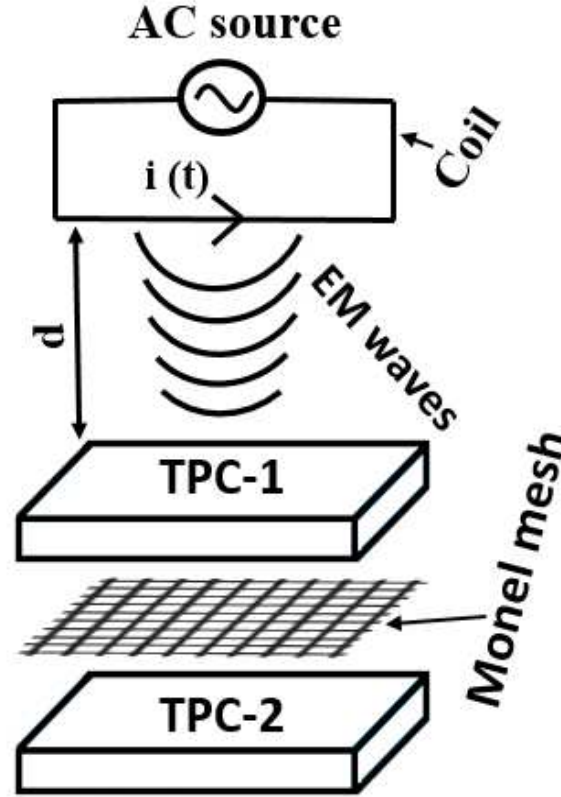
Figure 3.2: Overview of Simulation models.

Since, Monel contains 67% nickel and 27% copper its properties depend on its constituents. Relative Permeability, μ_r of nickel is in the range of $100 - 600$. Therefore, the relative permeability of Monel is assumed to be in the range of $350 - 400$, considering 67% nickel. Conductivity of Monel is assumed to be 3×10^7 (S/m), which is higher than nickel. The reason behind this is that Monel also has a considerable amount of copper.

22

Table 3.2: Properties of different materials used in the simulation models.

Material Name	Relative Permittivity ε_r	Relative Permeability μ_r	Bulk Conductivity, σ (S/m)	Dielectric Loss Tangent $\tan \delta$
Copper	1	0.99	5.8e7	0
Monel	1	350	3e7	0
Plexiglass	3.4	1	0	0.001

3.4 Simulation Modeling Approaches

Simulation models were created using a few different approaches. All different approaches used for modeling are discussed in detail in the following section.

3.4.1 Initial Approach

The basic steps for modeling are the same as shown in Figure 3.2. The first model for Monel mesh was created by using small polylines and then assigning them the property of circular cross-section. Polylines were used to create the Monel mesh as it appears in the real world, i.e., wavy and with both layers crossing each other and touching each other. This feature was achieved in Maxwell by constructing many small segments of polylines. There was no Plexiglass present in this model.
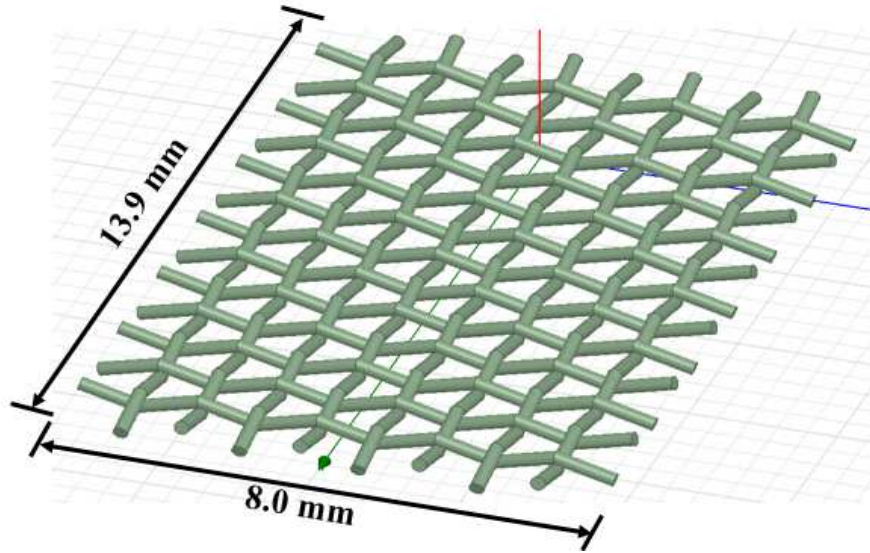
Figure 3.3: Wavy Monel mesh.

Figure 3.3 shows the Monel mesh created using small segments of polylines that are appropriately arranged to create a wavy mesh. The diameter of each rod is $250\,\mu m$. The dimensions of the mesh in the x and y directions are 13.9 mm and 8.0 mm, respectively. The simulation model did run and complete, and the obtained solid loss in the material found was **0.47 Watts**. Being the first model it was considered as a success. However, it was very time-consuming to create the model, and the solid loss obtained was very low. The reason behind this low solid loss is that there is no contact between the rods between layers. Means the wavy wire (rod) in the x-direction and in the y-direction are not touching each other, there is a tiny gap of around $0.01\,\mu m$ between the layers. This gap creates additional tetrahedras because the software is designed to create tetrahedras for the smallest dimensions in the model and thereby increasing the simulation runtime. Moreover, as there was no contact between the layers, the model does not fully represent the Monel mesh that are found in the real world.

3.4.2 Second Approach

Due to the limitation of the initial approach another approach was used. In the new approach, instead of creating a wavy mesh, a straight wire mesh was considered and created. Originally, there are two layers and each layer with conductor of 0.25 mm diameter. However, here trying to represent that same thing using single layer model so the diameter of the conductor is doubled (i.e., diameter is 0.5 mm). In addition, instead of using polylines, small segments of cylinders conductor were used to create the mesh.
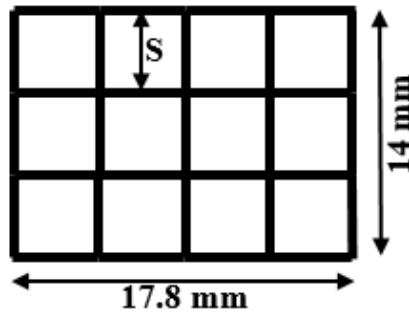
Figure 3.4: Small segments were used to create the mesh.

These cylindrical segments were arranged such that it will represent the mesh. Figure 3.4 shows how the mesh was created using small segments of cylinders. Each segment was 2 mm long, making the grid size (S) of 2mm. The diameter of the cylindrical rod segments was 0.5 mm. There were total 127 segments. The simulation did complete, and the solid loss obtained was **1.356 Watts**. This result clearly shows that using this approach (straight mesh) the solid loss obtained is significantly higher compared to the previous approach (wavy mesh). Moreover, the time required for creating models using this approach is minimal. Therefore, this approach was used for creating more models with different grid sizes.

25

3.4.2.1 50X50 Mesh per Square Inches

The two models discussed until now were created with random dimensions. Now, models were created using actual representative dimensions. The first Monel mesh simulated was 50X50 mesh per square inches. Here, the radius of the conductor is 0.1143mm, and the grid size is 0.28mm. Three models were created with different x and y dimensions (i.e., length and width).

Table 3.3: Results of three different size models for 50X50 mesh per square inches.

Structure Size (L by W)	No. of Segments	Solid loss (W) Without Plexiglass	Solid loss (W) With Plexiglass
5mm by 5mm	200	0.1626	0.02118
10mm by 10mm	800	1.1342	0.21627
15 mm by 15mm	1800	2.0693	0.52950

Table 3.3 shows the results obtained for six different models. Three models with Plexiglass and three models without Plexiglass. There are two Plexiglass blocks each with 3mm thickness, one above the mesh and one below the mesh as shown in Figure 3.2. As apparent, larger solid loss occurs with larger structure size because it increase the total overall resistance. For example, a 15 mm by 15 mm structure has over 2W of solid loss compared to 1W of solid loss for 10 mm by 10 mm structure. When Plexiglass materials are used on top and bottom of the mesh it reduces the solid loss. However, with an increase

26

in the dimension of the structure, hence, the overall Monel mesh the number of tetrahedras created also increases and because of that, the simulation runtime increases. Models with 20 mm by 20 mm dimension were also created, but the simulation did not complete because of limited computer memory.

3.4.2.2 40X40 Mesh per Square Inches

The next mesh studied was 40X40 mesh per square inches. The conductor radius is 0.4699mm, and the grid size is 0.0825mm. Results for the 40X40 models and comparison of these results with 50X50 mesh are shown in Table 3.4.

Table 3.4: comparing results of 50X50 mesh with 40X40 mesh.

Structure Size (L by W)	Solid loss (mW) With Plexiglass 50X50 mesh	Solid loss (mW) With Plexiglass 40X40 mesh
5mm by 5mm	21.184	18.2
10mm by 10mm	216.27	196.1
15 mm by 15mm	529.50	497.5
20 mm by 20 mm	-	785.21

Results from Table 3.4 show that the solid loss value for 50X50 mesh in the presence of Plexiglass is higher compared to 40X40 mesh for all different dimensions. The

27

comparison for 20 mm by 20 mm dimension is not clear because the simulation did not complete for the 50X50 mesh. This comparison proves that if there are more meshes per square inches, the solid loss value is higher. Therefore, 100X100 mesh per square inches was studied next. In this simulation model, there were more than 7000 segments. The simulation model for 100X100 mesh did not complete because of limited memory of the computer.

3.4.3 Third Approach

With Monel 400, a 40X40 mesh is the commonly used mesh in welding two parts of thermoplastics. Therefore, more models were created to study this mesh in detail. A third approach was used to create such mesh so that the simulation runtime is not prohibitive. The process to create such mesh using this approach is as shown in Figure 3.5.
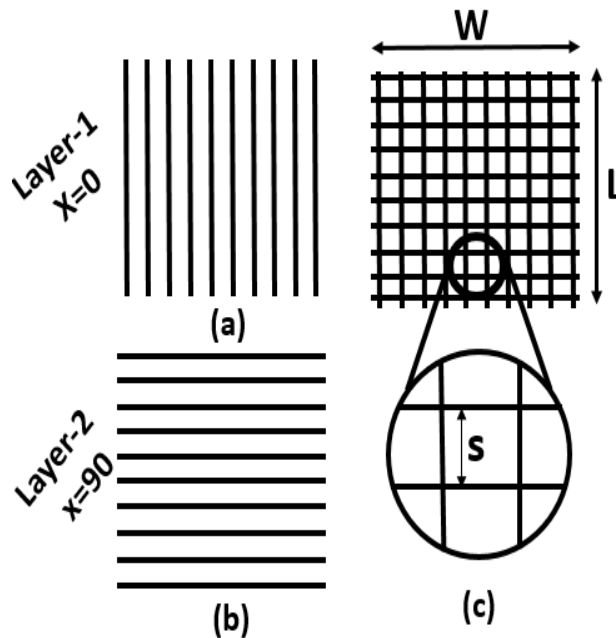
Figure 3.5: (a) layer 1 (b) layer 2 (c) grid.

28

First, Monel rods in layer 1 are created as shown in Figure 3.5(a) (rods are vertical). The radius (r) of each rod is 0.127mm. Next rods were created in layer 2 as shown in Figure 3.5(b) (rods are horizontal). This way a grid structure was obtained (see Figure 3.5(c)) where the other parameters were: length (L) and width (W) of 25mm, and spacing (S) of 0.381mm. Spacing (S) is the surface to surface distance between two adjacent rods as shown. All of these parameters (r, L, W, S) are different for different mesh models. The conductors on each surface touches each other, so there is no gap between the layers. Once, the two layers are on top of each other it creates a mesh structure with our desired spacing/grid size. The total thickness of the mesh with both layers combined is 0.508 mm. The name of this mesh is Monel 400 (40X40 mesh per square inches). A total number of meshes per square inches are 1600. In x-direction, there are 40 meshes in a straight line, and there are 40 such lines in the y-direction.

Once the mesh and the Plexiglass slabs were created, now it was time to create the model of the coil. A square coil was used for all models discussed above. However, for this model special coil was designed to emulate the coil in the experiments. Figure 3.6 shows the coil dimensions and how it was created.

The coil created is shown in Figure 3.6. The coil is designed to match the coil in the experiments, but other coil shape and sizes were also simulated. The coil shown above was made using copper as the conductor. As shown in Figure 3.6, the total length of the coil is 67.35 mm, and the diameter is 6.35 mm. The diameter of the hollow section is 3.302 mm. The construction of the coil in Maxwell software is done as follow; first, a solid conductor was created, and then another conductor was created with a smaller diameter. The smaller diameter conductor was subtracted from the larger diameter and then a hollow

conductor coil was created. As shown in Figure 3.6, there is a gap of 25mm between two inner edges of the coil. The coil is placed precisely above mesh, covering full mesh with this edge-to-edge distance.
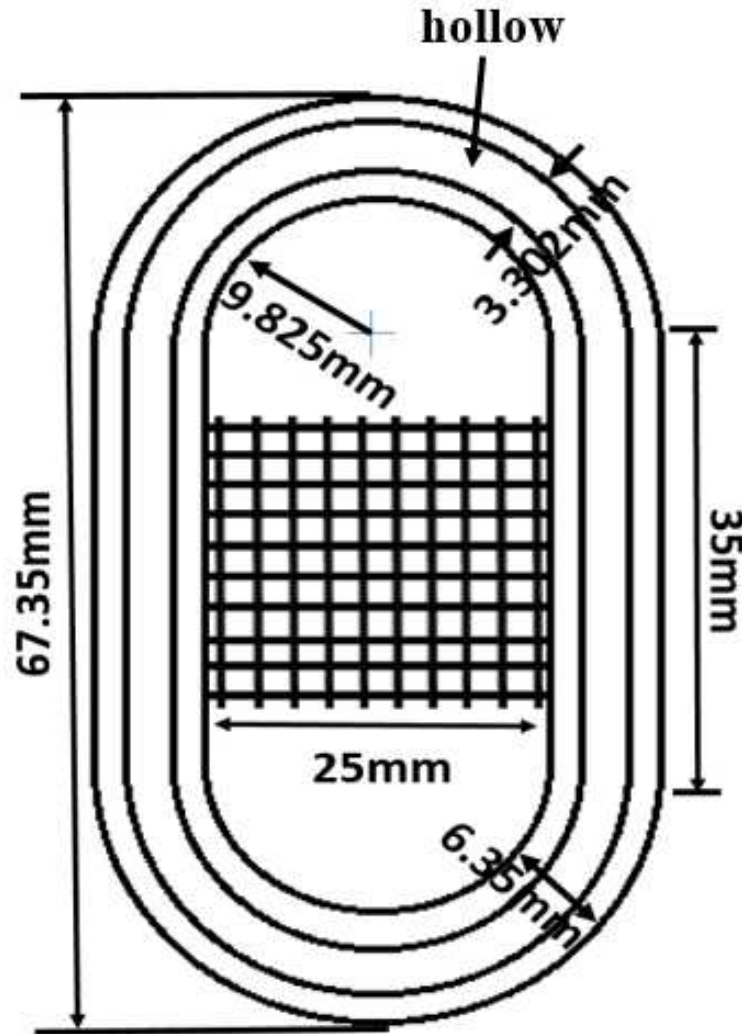
Figure 3.6: Hollow copper coil

In the end, the boundary condition is assigned to a finite region around the whole model. The coil is excited using 500 A AC current at a frequency of 292 KHz.

30

3.4.3.1 Results

Once the simulation is completed, different fields can be plotted on the mesh, and the value of the solid loss can be obtained. Solid loss value from the simulation is **2.565 Watts**, and this is averaged value of the entire model. The solid loss at each intersection points between the two layers can be calculated if the current density at those locations is known. Current density is calculated by plotting markers on the current density plots at all those locations. Once, the solid loss at all the intersection points are calculated, the change in temperature at all those points is calculated using formulas discussed later in this section.
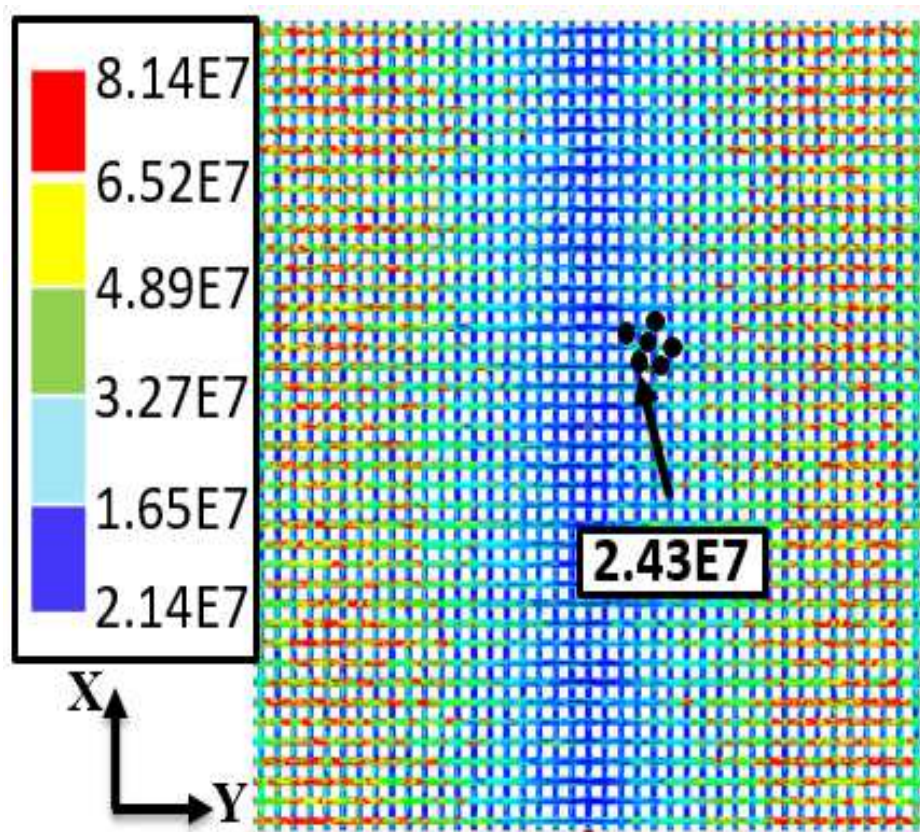
(a)
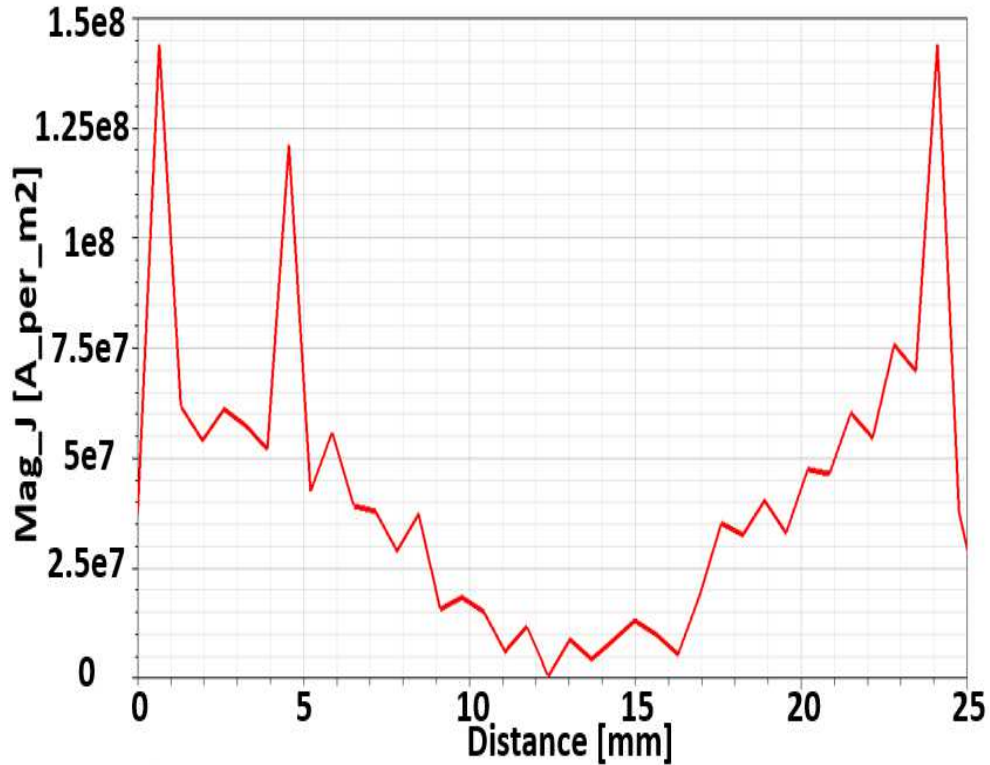
(b)

Figure 3.7: Results of (a) current density plot on mesh, (b) distribution of "J" in one of the Monel rod along the length in the Y-direction.

The current density plot shows the distribution of "J" across the whole mesh. Figure 3.7 shows the distribution of "J" along the length of one of the horizontal (Y-direction) rod out of many. Current density values are minimal in the center, and it increases as we move away from the center in either direction. Distribution on both sides is almost identical. Distribution of heat is the same as the distribution of "J" because temperature is directly proportional to "J." The values of "J" at any point on the mesh from this current density plot can be calculated using markers. Now, using these values of "J," the change in temperature can be calculated as shown in the following section.

3.4.3.1.1 Calculation of Change in Temperature Using Current Density Value:

Step 1: Calculate current from current density:

$$I = \vec{J} \times \pi \times r^2 \text{ (Amps)} \dots (3.1)$$

I = current, $\vec{J}$ = current density, r = radius of Monel rod

Step 2: Calculate resistance:

$$R = \frac{R_s}{2 \times \pi \times r} \text{ (Ohms)} \dots (3.2)$$

R = Resistance, R_s = Surface Resistance

$$R_s = \sqrt{\frac{\omega \times \mu}{2 \times \sigma}} \text{ Ohms} \dots (3.3)$$

σ = Conductivity, ω = angular frequency, μ = Permeability, $\mu = \mu_0 \mu_r$

Step 3: Calculate loss

$$Loss = I^2 \times R \text{ (Watts)} \dots (3.4)$$

Step 4: Now, calculate the change in temperature (ΔT):

$$\Delta T = \frac{E}{m \times C} \text{ (}^\circ C \text{)} \dots (3.5)$$

E = energy, m = mass, C = heat capacity of Monel

Energy (E) = Loss x time (Joules) time = in seconds,

33

Mass (m) = density of Monel x Volume (grams)

From Figure 3.7, the value of $\vec{J}$ is 2.43E7. The heat capacity of Monel is considered to be $0.427 J/g-°C$ and the density of Monel is $8.80 g/m^3$ [24]. Change in temperature is calculated for 1 second of exposure using all of the above-mentioned equations and the calculated value for ΔT ($°C$) is 36.60. The assumption here is that 100% of the energy lost is used to heat the mesh. However, if only a certain percentage of energy lost is available as heat, ΔT will be much smaller as shown in Table 3.5.

Table 3.5: Change in temperature with a different percent of energy lost available as heat.

Markers	**Current density** (A/m²)	**ΔT ($°C$)** 100%	**ΔT ($°C$)** 75%	**ΔT ($°C$)** 50%	**ΔT ($°C$)** 25%
1	3.963e7	97.33	72.99	48.66	24.33
2	3.694e7	84.56	63.42	42.28	21.14
3	3.059e7	57.99	43.49	28.99	14.49
4	2.969e7	54.63	40.97	27.31	13.66
5	2.43e7	36.60	27.45	18.30	9.15
6	2.254e7	31.48	23.61	15.74	7.87

Table 3.5 shows the results of the change in temperature for different markers shown in Figure 3.7 (a). Moreover, it shows the results for 100 percent to 25 percent energy

34

loss is used for heating the Monel mesh. The percent results is presented here with consideration that in the event that there is a cooling mechanism to which the heat is loss then only a certain fraction of the heat will actually be utilized for the welding. In the experiment, the precise location of the thermocouple was not known; hence, few markers were placed in different locations as shown in Figure 3.7 (a).

3.5 Experiment

An experiment was performed to compare the simulation results with experimental results. Here, all the setting was kept as close as possible to that used in the simulation.

3.5.1 Experimental Setup

In the experiment, the set-up was made as close as possible to that of the simulation model. A Plexiglass slab of length 200 mm, width 50 mm, and thickness 3 mm was placed on a flat table, on top of which the Monel mesh was placed. The mesh was placed at one location on top of the Plexiglass using tape. An E-type thermocouple was glued at a specified location on the mesh. The thermocouple location was just above the center on the right side. Second, another Plexiglass slab was placed on top of the Monel mesh, and the whole setup was made airtight by covering it with a nylon bag. The coil was precisely held stationary above the mesh with the help of a robot.

As shown in Figure 3.8, the two ends of the coil are connected to AC source and the coil was precisely held stationary above the mesh with the help of a robot. The coil used in the experiment had more number of arms than that in the simulation soil, with the distance between two arms being 25mm. Only two arms of the coil were used for heating the mesh, same as shown in Figure 3.6. The other arms of the coil were at some distance

from the mesh hence they were will not expected to contribute to the heating of the mesh. In addition, an IR camera was placed on top to capture the temperature on the mesh as well.
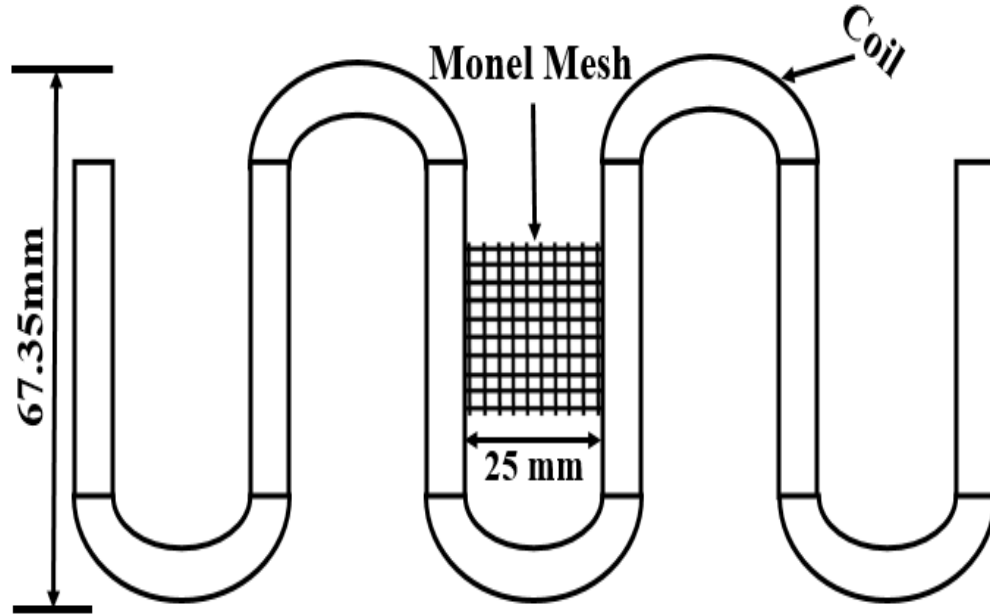
Figure 3.8: Experimental coil on top of Monel mesh.

3.5.2 Experimental Results

A 500 Amp AC current with 292 kHz frequency was applied to the coil. Temperature data was recorded using both the thermocouple and the IR camera. As mentioned, the exposure time was 1 second. The thermocouple reading was around $40\,^{\circ}C$, and the reading from the IR camera was $44\,^{\circ}C$. Moreover, the heat distribution on the mesh appears to be the same as was seen in the simulation result. There is less heating in the center of the specimen while there is more heating at the edges. Figure 3.9 shows the reading obtained using the IR camera.

36

Figure 3.9: IR camera reading

It the end, welding two thermoplastic composites using induction heating was achieved. The weld was proper and firm. Heat distribution on the mesh is as shown in Figure 3.7 (a), the result from an IR camera confirmed it. Heat is less at the center, and it increases as we move away from the center in either direction. As the temperature values are high on both sides that will melt the susceptor and some portion of the thermoplastics. Once it cools down, the welding process is complete.

The values of change in temperature from all three different methods that is (1) simulation, (2) IR camera, and (3) thermocouples were close. In the simulation model, the coil was at a fixed location, but in actuality, there is a moving coil to weld extended parts of the thermoplastics. This part is not done because it was not possible to create simulations with moving coil.

CHAPTER 4

THEORETICAL NEAR-FIELD CURRENTS FOR INDUCTIVE THERMOPLASTIC WELDING

4.1 Introduction

Mathematical equations were derived to understand the results obtained from Ansys Maxwell simulations. Moreover, the simulation does not give the temperature value as an output. Therefore, formulas were derived to overcome that problem. In this chapter, Biot-Savart law is explained in detail. Equations used to find a change in temperature is also explained in detail. Also, a comparison is made between the simulation results with analytical results.

4.2 Biot-Savart's law

The Biot-Savart law is a mathematical representation of the vector magnetic field intensity, $\vec{H}$ or flux density, $\vec{B}$ near a current carrying conductor. For example, $\vec{B}$ at a point, P is given by,

$$\vec{B} = \frac{\mu_0 I}{4\pi} \int \frac{\vec{dl'} \times \hat{a}_R}{R^2} \ \dots \ (4.1)$$

Where $\mu_0 = 4\pi \times 10^{-7}$ (H/m) is the free-space permeability, I is the current flowing in the wire in amperes, $\vec{dl'}$ is vector current length element in the direction of the

38

current, $\hat{a}_R$ is the unit vector from the source point to the field point, and R is the scalar distance from $\vec{dl}'$ to point P.

Using this law, magnetic flux density at a fixed point and an arbitrary point in space due to a current carrying wire of finite length can be calculated. Equations for both the cases mentioned above are explained in the next section.

4.2.1 Magnetic Flux Density at Fixed Point $P(r,0,0)$

Figure 4.1 illustrates a current carrying wire of length, $2L$ symmetrically placed along the Z-axis. Magnetic flux density, $\vec{B}$ at point P located at a distance r from the wire could be calculated using Equation (4.1).
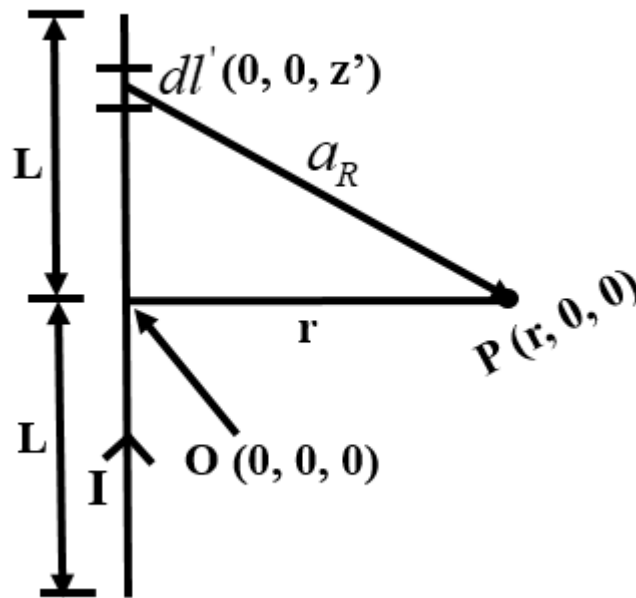
Figure 4.1: Representative case 1: $\vec{B}$ **at a fixed-point P.**

For a differential element, equation (4.1) can also be written as

$$d\vec{B} = \frac{\mu_0 I}{4\pi} \left(\frac{d\vec{l}\,' \times \vec{R}}{r^3} \right) \dots (4.2)$$

After solving Equation (4.2), $\vec{B}$ can be expressed as

$$\vec{B} = \hat{a}_\phi \frac{\mu_0 IL}{r 2\pi \sqrt{L^2 + r^2}} \dots (4.3)$$

4.2.2 Magnetic Flux Density at an Arbitrary Point P (x, y, z) in Space

The formulation described in the previous section has a limitation in terms of finding $\vec{B}$ at a specific point as explained in the previous section. In this section, formulation to find $\vec{B}$ at an arbitrary point $P(x, y, z)$ is derived. Consider the scenario illustrated in Figure 4.2.
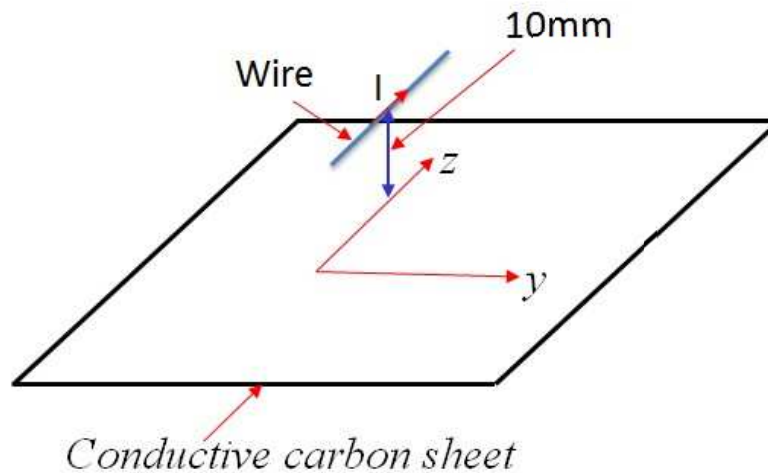
Figure 4.2: Representative case 2: Find $\vec{B}$ at any point on the yz-plane.

40

Magnetic field intensity, $\vec{H}$ at any point in space located at a distance, x from a current carrying wire of length, $2L$ is given by

$$\vec{H}_y = \frac{I \cdot x}{4\pi\left(x^2 + y^2\right)}\left\{\frac{(z+L)}{\sqrt{x^2 + y^2 + (z+L)^2}} - \frac{(z-L)}{\sqrt{x^2 + y^2 + (z-L)^2}}\right\} \; \dots \text{(4.4) with}$$

$$\vec{B} = \mu_0 \vec{H} \; .$$

Now, once magnetic field intensity $\vec{H}$ is calculated. Current density is calculated using the values obtained from magnetic field intensity using Equation (4.5).

$$\vec{J}_s = \hat{n} \times \vec{H}_y \; \dots \text{(4.5)}$$

$\vec{J}_s$ is current density, $\hat{n}$ is the outward normal

Calculating the current density is very important because the outputs from Ansys Maxwell simulation are current density plots/values and solid loss value. Now, using equations (4.4) and (4.5), magnetic field intensity, $\vec{H}$ and current density, $\vec{J}_s$ can be calculated at any point on the yz-plane.

4.3 Results

A Matlab script was developed to calculate the current density and power loss on the sheet. In Matlab, 3000 (S/m) conductivity was used for the carbon fiber material. Figure 4.3 shows the results where $I = 500 A$ was used.

41

(a)

(b)

(c)
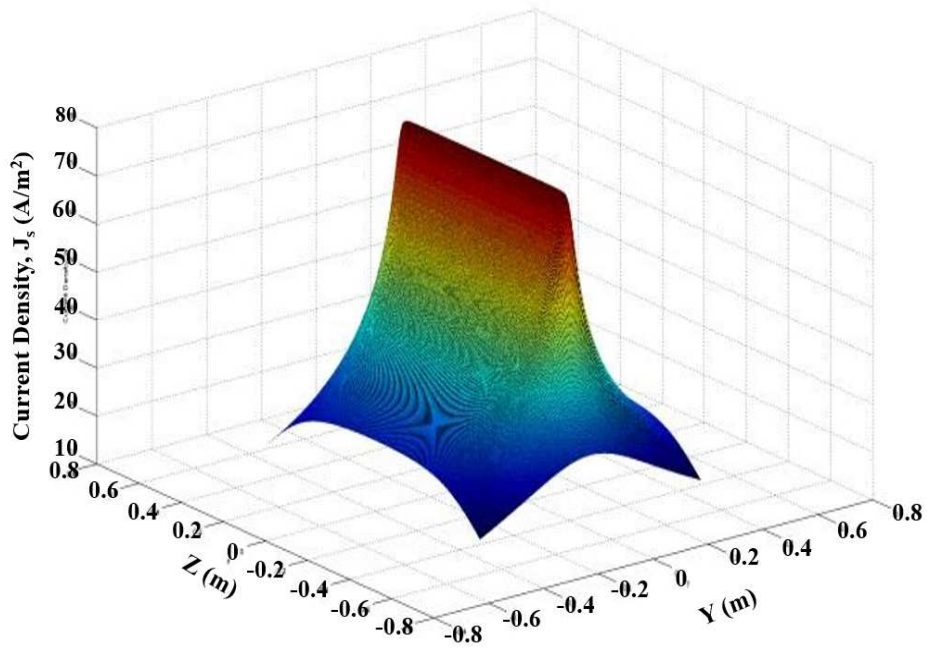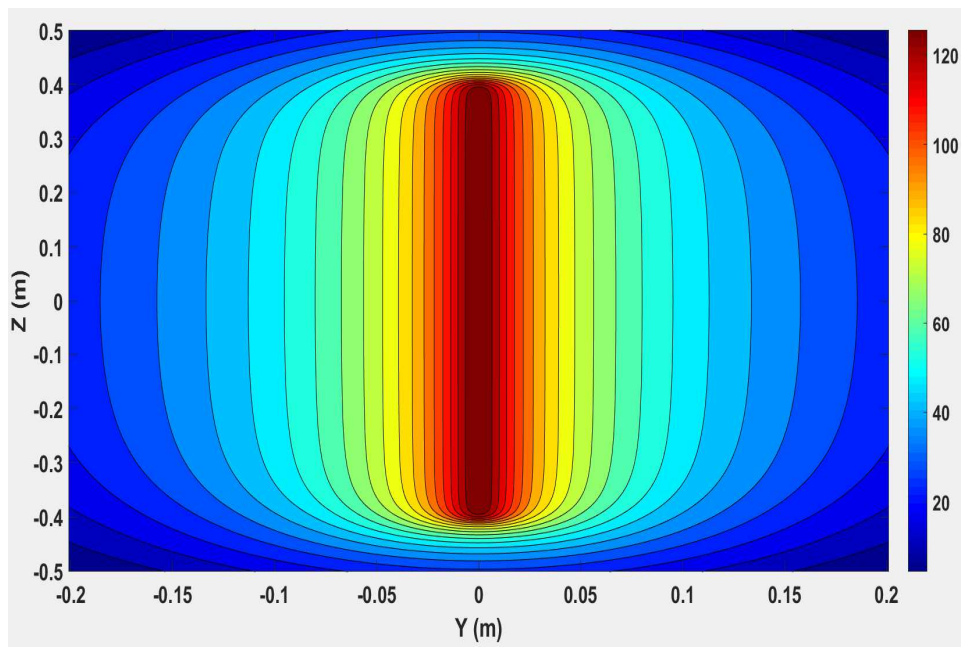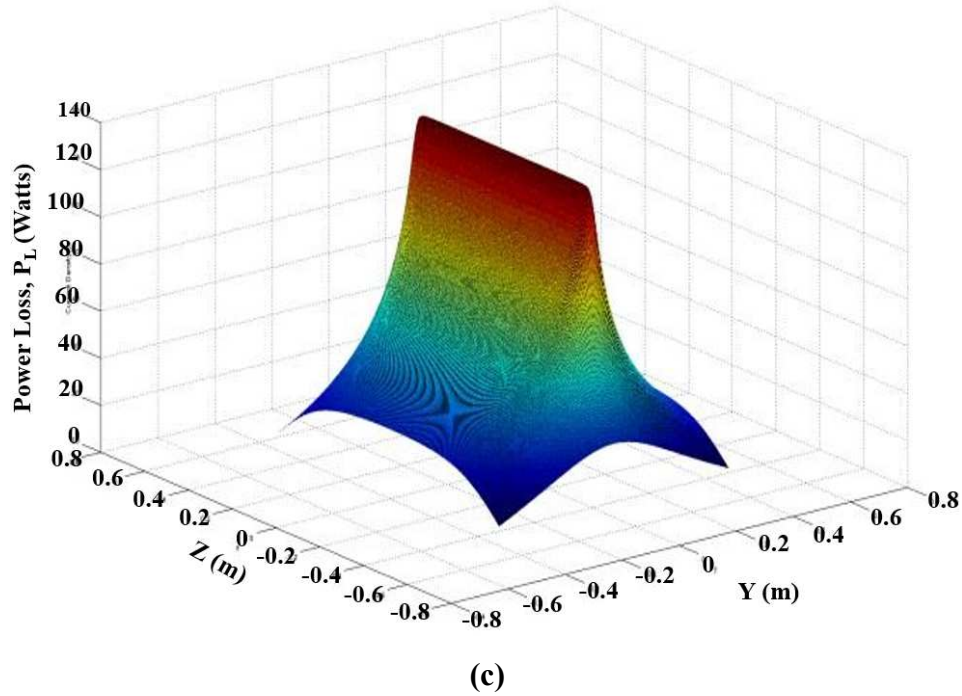
Figure 4.3: MATLAB code results on the sheet (a) surface plot of current density, (b) contour plot of current density, and (c) surface plot of power loss considering a carbon sheet with conductivity of 3000 (S/m).

Figure 4.3 shows that current density and power loss values are maximum at the center, right below the current carrying wire. Also, as we move away from the center in either direction the value of current density and power loss decrease. From Figure 4.3 (a) and (c), it is clear that the current density is directly proportional to the power loss. Power loss plot is calculated from current density plot using the equations shown in section 3.4.3.1.1.

4.4 Comparison between Analytical Results vs Simulation Results

To understand how Maxwell software solves the equations, a comparison between analytical results with simulation results was studied. This comparison was carried out for

43

a straightforward model to avoid any complicated analytical calculations. Here, the analytical approach, the simulation approach, and then the comparison at the end are discussed.

4.4.1 Analytical Approach

Using the concept of Bio-Savart's law, that magnetic field intensity, $\vec{H}$ at an arbitrary point in space due to a current carrying wire can be calculated using Equation 4.4. The analytical model set up is shown in Figure 4.4.
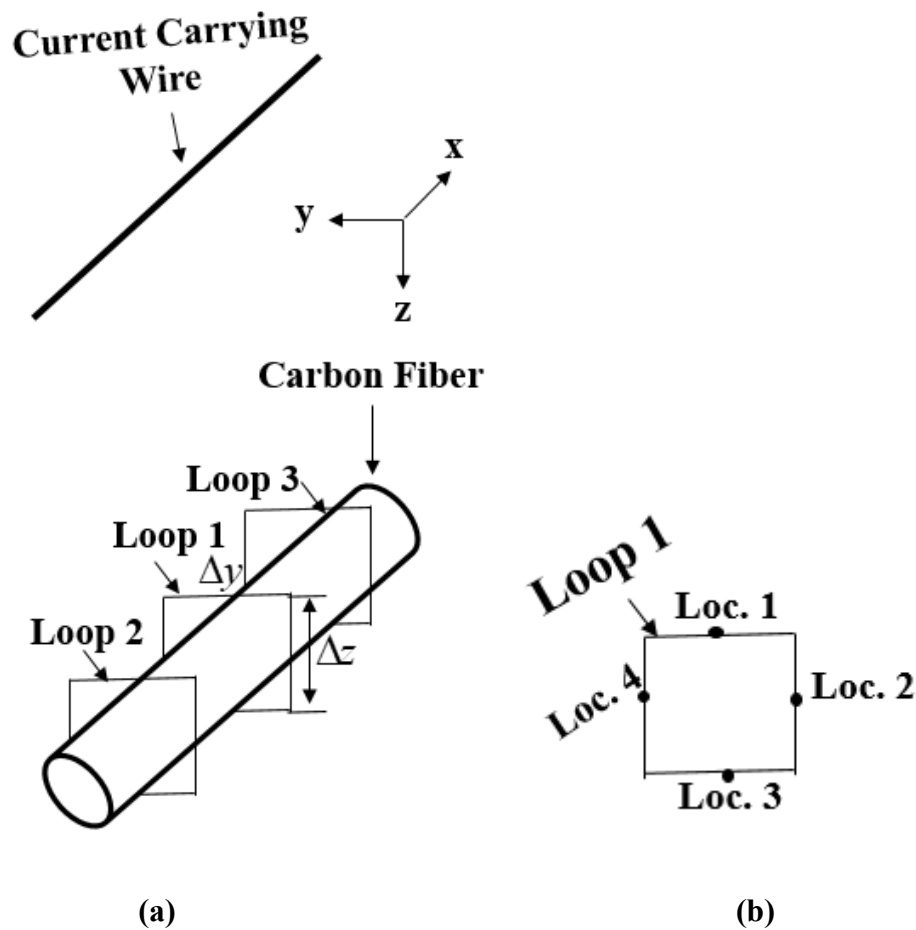

(a)   (b)

Figure 4.4: Analytical model (a) setup, (b) four locations of integral Loop 1.

In this model, a 5 mm long current carrying wire, and a carbon fiber are separated by 5.21 mm distance. The length and diameter of the carbon fiber are 5mm and 2mm, respectively. The hypothetical integration paths e.g. the square loops are 0.01mm away from the surface of the fiber. Therefore, the length of each side of the integration loops is 2.01 mm. To calculate the current induced on the fiber due to the currents on the wire, first, the magnetic field intensity, $\vec{H}$ near the fiber at different locations are calculated. Then the current on the fiber is calculated by applying Ampere's law (a line integral around the fiber as shown in Figure 4.4 (a)). Once $\vec{H}$ is calculated, an induced current is calculated using Equation (4.6). There are three integral loops for three different points on the fiber. Figure 4.4 (b) shows the location on Loop 1 where magnetic field intensity is calculated. Similarly, for Loop 2 and Loop 3, the locations are loc.5, loc.6, loc.7, loc.8 and loc.9, loc.10, loc.11, loc.12, respectively. To find current values at other locations on the fiber, more loops will be needed to be created at all those locations.

The equations to find currents at particular points on the fiber is given by

$$I = \left(\vec{H}_y \Delta y\right) + \left(\vec{H}_z \Delta z\right) + \left(\vec{H}_y \Delta y\right) + \left(\vec{H}_z \Delta z\right) \ldots (4.6)$$

Magnetic field components $\vec{H}_y$ and $\vec{H}_z$ are two unknown variables in (4.6). The square loop has four sides; a magnetic field at the center of each side is calculated. These center locations are as shown in Figure 4.4 (b). When solving for y-direction sides, $\vec{H}_y$ is multiplied with the length of that side, i.e., Δy. During y-direction solutions, $\vec{H}_z$ value is zero.

Similarly, it will be the case when solving for z-direction sides. Once magnetic field intensity $\vec{H}$ is calculated on all sides, those values will be multiplied with the length of their respective sides. The sum of all four sides will yield the induced current at that point on the fiber.

Equations to find the magnetic field components ($\vec{H}_y$ and $\vec{H}_z$) are derived using Biot-Savart's law and the approach is the same as discussed earlier. Final expressions for the magnetic field components are given as,

$$\vec{H}_y = \frac{I \cdot z}{4\pi\left(z^2 + y^2\right)}\left\{\frac{(x-L)}{\sqrt{z^2 + y^2 + (x-L)^2}} - \frac{(x+L)}{\sqrt{z^2 + y^2 + (x+L)^2}}\right\} \quad \dots (4.7)$$

$$\vec{H}_z = \frac{I \cdot y}{4\pi\left(z^2 + y^2\right)}\left\{\frac{(x+L)}{\sqrt{z^2 + y^2 + (x+L)^2}} - \frac{(x-L)}{\sqrt{z^2 + y^2 + (x-L)^2}}\right\} \quad \dots (4.8)$$

Here, x, y, z are coordinates of the points, L is the length of the wire, and I is the current flowing in the wire in A. Results obtained using the analytical method are discussed in the comparison section.

4.4.2 Ansys Maxwell Simulation Model

A simulation model was also created using Maxwell to emulate the analytical model. The simulation model is as shown in Figure 4.5.

46
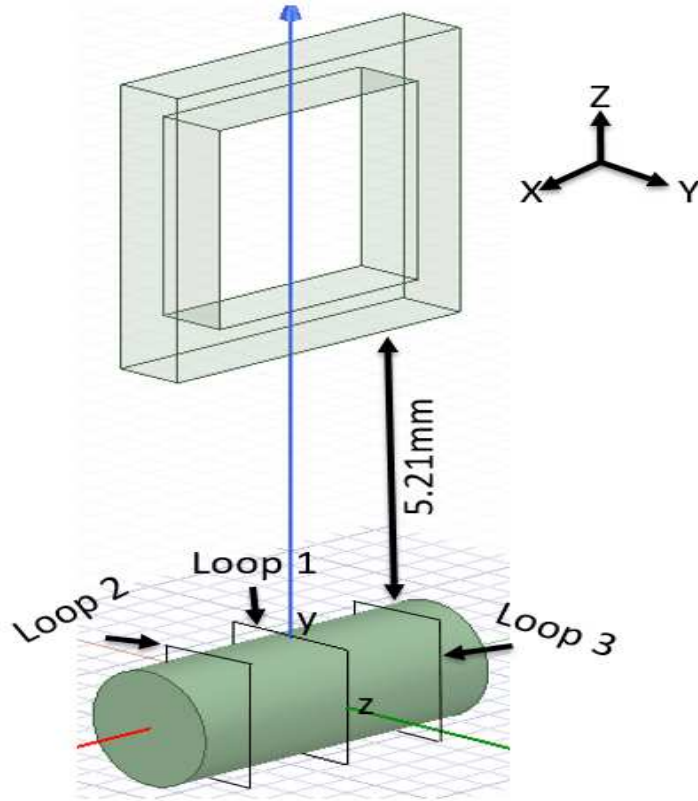
Figure 4.5: Simulation model

The source is a square coil with four arms (two vertical and two horizontal). The cross section of the conductor coil is square with sides of length 1 mm. A single fiber is placed below the coil. The fiber is 5 mm long, and the diameter is 2 mm. Copper is used as the material of fiber because the properties of copper are standard, and no assumption is required. The bottom of the coil is 5.21 mm away from the top of the fiber. Three loops are created around the fiber to find the current at those particular points using line integration. Loop 1 is at the center of the fiber and loop 2 and loop 3 are at the same distance from the center on respective sides. This arrangement is identical as in analytical setup.

47

The coil is excited with an AC current of 500 A at a frequency of 292 KHz. Once the simulation is complete, the magnetic field intensity graph is plotted on the fiber. Using markers, the value of magnetic field intensity $\vec{H}_y$ are calculated at the same locations as shown in the analytical model Figure 4.4. Once magnetic field intensity values are calculated on each side of the square loops, Equation (4.6) is used to find the currents at those locations. Results obtained using the simulation approach are discussed in the comparison section.

4.4.3 Result Comparison

The results from analytical as well as those from simulation models are compared in this section. Two different cases of the results are compared. In the first case, the analytical calculation results have only one piece of the wire while the simulation has all four arms of the coil. In the second case, the analytical calculation results have four pieces of the wire and, the simulation has four arms of the coil.

There are four values for each integral loops as shown in Table 4.1. Two values for $\vec{H}_y$ component and two values for $\vec{H}_z$ component. The plots are generated for analytical and simulation results using values shown in Table 4.1. The plots are shown in Figure 4.6.

Figure 4.6 shows the $\vec{H}$ field components ($\vec{H}_y$ and $\vec{H}_z$) values using the formulas on all the three loops. While calculating analytically, there is a single piece of the wire carrying a current. However, it is not the same in the simulation where there are four arms of the coil. Hence, when comparing the two plots of Figure 4.6 (a) and (b), the trend of the

48

graph looks similar. However, the values obtained from the analytical calculation are remarkably higher than those from the simulation values.
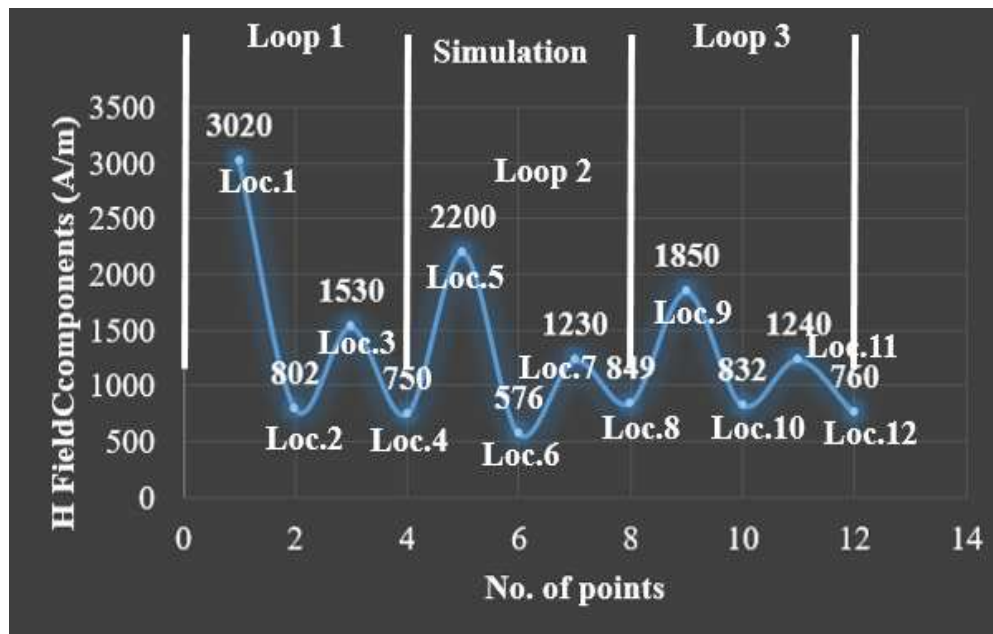
Table 4.1: Comparison of analytical values with simulation values obtained for case 1.

Comparison	Analytical		Simulation	
	$\vec{H}_y$ (A/m)	$\vec{H}_z$ (A/m)	$\vec{H}_y$ (A/m)	$\vec{H}_z$ (A/m)
Loop 1	6600 3600	716 716	3020 1530	802 750
Loop 2	5720 3300	642 642	2200 1230	576 849
Loop 3	5720 3300	642 642	1850 1240	832 760

The reason behind this mismatch of values could be the three extra arms of the coil in the simulation. To verify this a second approach was studied. In the second case, there were four pieces of wires instead of a single piece of wire for the analytical approach. The simulation model remains the same as shown in Figure 4.5. The new set up for the analytical approach is shown in Figure 4.7.
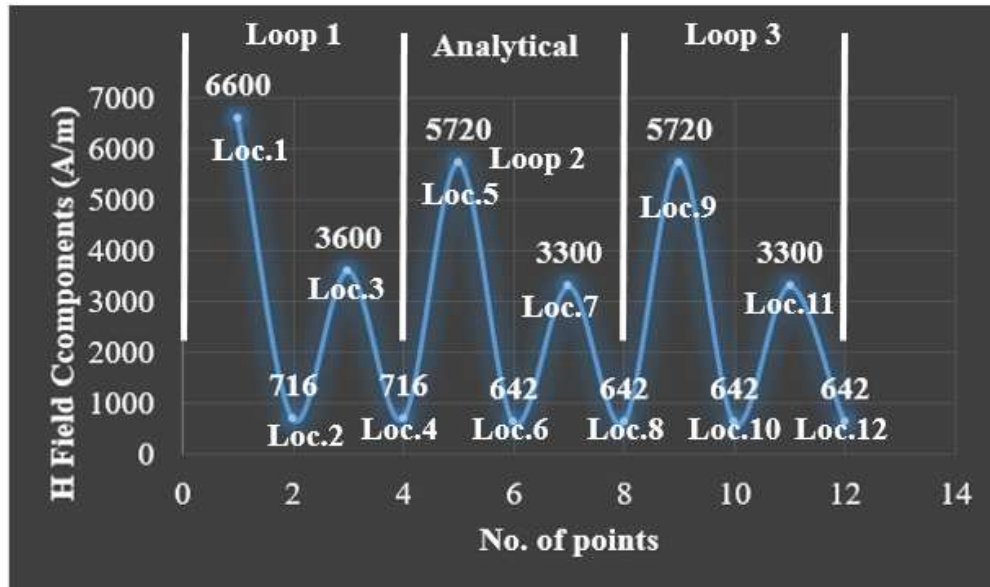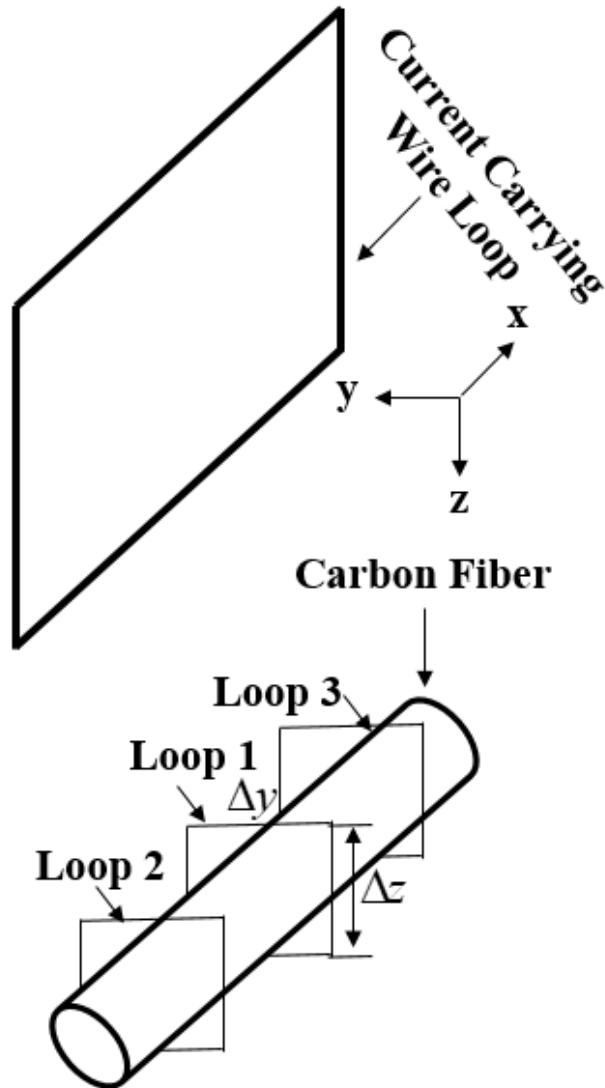
(a)

(b)

Figure 4.6: comparing the plot of analytical values with simulation values, (a) plot of analytical values with one piece of the wire, (b) plot of simulation values with all four arms of the coil.

Figure 4.7: Analytical setup with four pieces of current carrying wire.

The entire model is the same as in Figure 4.4 with the only difference being that here there are four pieces of wires instead of a single piece of wire. These four pieces of wires are arranged such that together they represent the coil as shown in the simulation model. In this setup, there are four pieces of wires (two vertical and two horizontal). Equations to find the magnetic field components values due to the horizontal pieces of the wire have already been derived as shown in Equation (4.7) and (4.8). Now, the equations

to find the magnetic field components values due to the vertical pieces of the wires needs to be derived. The derivation approach is the same as discussed earlier in this chapter, using Biot-Savart's law. Once the derivation is complete, there will be four equations for finding magnetic field components. Two equations for horizontal arms and two equations for vertical arms.

$$\vec{H}_y = \frac{I \cdot x}{4\pi(x^2 + y^2)} \left\{ \frac{(z+L)}{\sqrt{x^2 + y^2 + (z+L)^2}} - \frac{(z-L)}{\sqrt{x^2 + y^2 + (z-L)^2}} \right\} \quad \dots (4.9)$$

$$\vec{H}_x = \frac{I \cdot y}{4\pi(x^2 + y^2)} \left\{ \frac{(z-L)}{\sqrt{x^2 + y^2 + (z-L)^2}} - \frac{(z+L)}{\sqrt{x^2 + y^2 + (z+L)^2}} \right\} \quad \dots (4.10)$$

Results obtained analytically for the same three loops with new setup are shown in Table. 4.2. The plots are generated for analytical and simulation results are shown in Figure 4.8.

In this comparison, there are four pieces of wires for the analytical calculations. The trend in the plot is still almost identical for both the analytical and the simulation plots. Moreover, the difference between the values is less compared to that of case 1. Even though the results are getting closer for both analytical and simulation approaches, but still the results are not matching exactly. It was found out that the two vertical arms do not affect the results because in both the verticals wires current flows in opposite directions hence, the magnetic fields generated by both vertical arms get canceled.

Table 4.2: Comparison of analytical values with simulation values obtained for case 2.

Comparison	Analytical		Simulation	
	Hy (A/m)	Hz (A/m)	Hy (A/m)	Hz (A/m)
Loop 1	4460	880	3020	802
	2136	880	1530	750
Loop 2	3162	798	2200	576
	1656	798	1230	849
Loop 3	3162	798	1850	832
	1656	798	1240	760
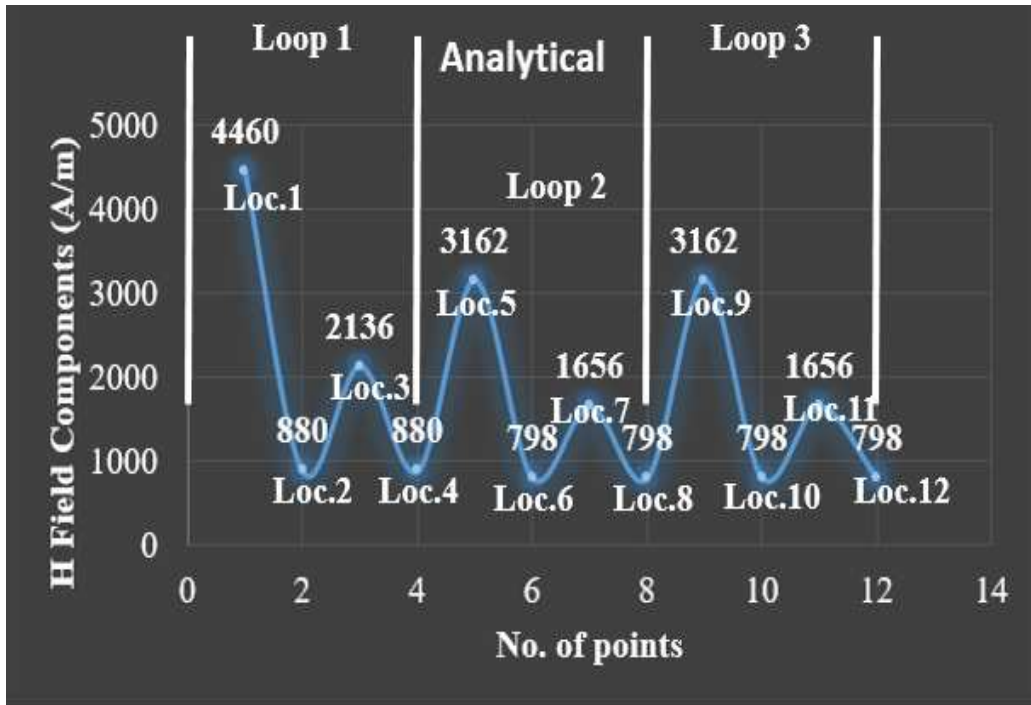
(a)
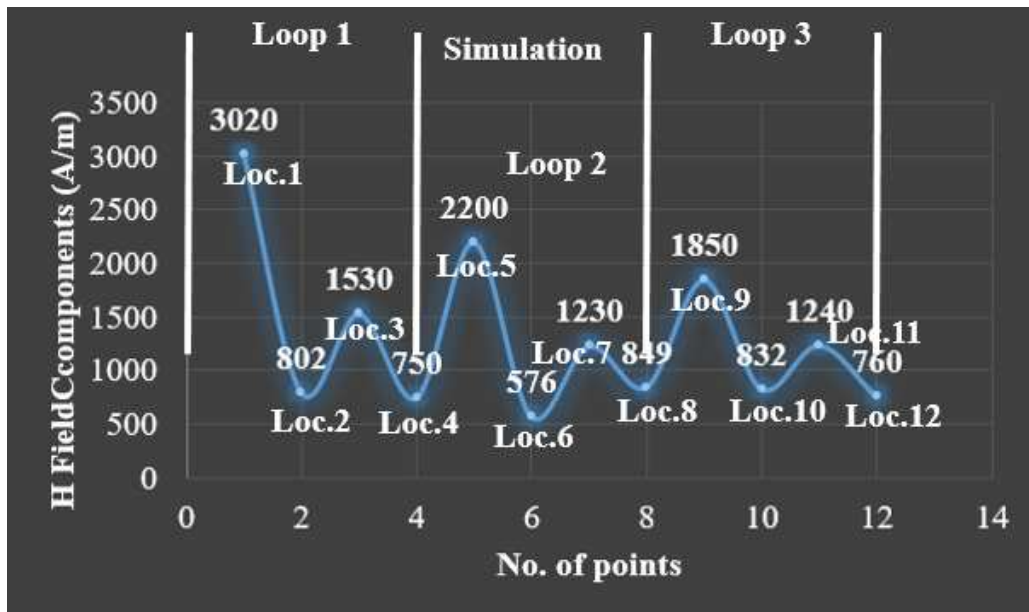
(b)

Figure 4.8: comparing the plot of analytical values with simulation values considering all four arms of the coil, (a) plot of analytical values, and (b) plot of simulation values.

The reason for this mismatch could be that in the simulation the coil is fabricated using rectangular blocks. Smaller rectangular block was subtracted from larger rectangular block, so the conductor has a square cross section with each side of length 1 mm, whereas, there was no diameter in the wire used for the analytical calculations. The equations used for the analytical calculations do not vary with the diameter of the wire. In addition, there was no role of the fiber in the analytical calculation because the equations do not depend on the presence of the fiber. On the other hand, in the simulation because of the presence of the fiber (copper as material), it is assumed that the induced current on the fiber will have its own magnetic field, which will oppose the magnetic field induced due to the coil. Hence, the simulation results values are less compared to the analytical values.

55

CHAPTER 5

RF/ELECTROMAGNETIC MODELING AND ANALYSIS OF THE RF HEATING OF CARBON FIBER COMPOSITE MATERIALS

5.1 Introduction

In recent years, the use of Carbon fiber reinforced composites (CFRC) has increased tremendously in the field of aerospace and automotive industries as a replacement for metals due to their high strength and light weight properties [26]. CFRCs are realized by infusing a matrix of resin into high strength carbon fibers that are embedded and aligned along a preferred direction of reinforcement. Carbon fibers are usually combined with other materials to form a composite. When impregnated with a plastic resin and baked it forms a carbon fiber reinforced composite (often referred to as carbon fiber) [27]. The binding polymer is often a thermoset resin such as epoxy, but other thermoset or thermoplastic polymers, such as polyester, polyphenylene sulfide (PPS), polyetherketoneketone (PEKK), polyetheretherketone (PEEK) and many more could also be used.

Despite the many mechanical advantages, composite materials are not as electrically conductive as metals such as aluminum and titanium. It has an electrical conductivity that is nearly 1000 times lower than that of most metals [28]. Carbon fiber reinforced composites (CFRC), are extremely strong and lightweight fiber-reinforced polymers. CFRCs can be expensive to produce but are commonly used wherever high strength-to-weight ratio and rigidity are required, such as aerospace, automotive, etc. [29].

Carbon fiber composites are about 10 times stronger and 5 times lighter than steel, and about 1.5 times lighter than aluminum. Together with the right resin systems, carbon fiber composites are also known for being extremely corrosion resistant and able to withstand high wear [27]. Carbon fibers are 5-10 micrometers in diameter and are composed of mostly carbon atoms.
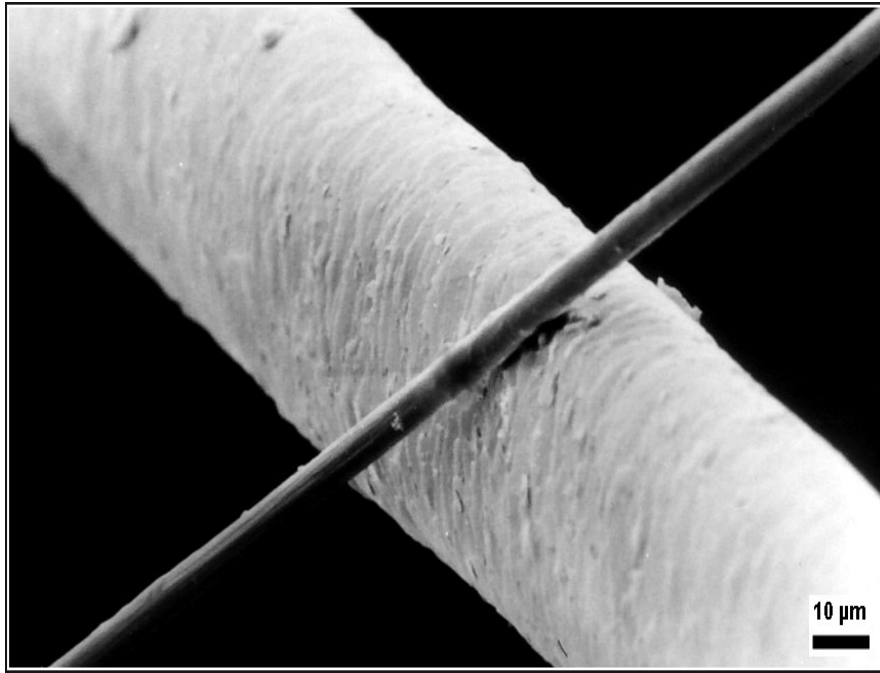

Figure 5.1: A 6 micrometer diameter carbon filament (running from bottom left to top right) compared to a human hair [27].

A single carbon fiber is compared with a human hair in Figure 5.1. The average diameter of a human hair is in the range of 20 to 100 micrometer.

In this chapter, different heating mechanisms of carbon fiber composites are studied. Ansys Maxwell simulations were performed to study different parameters that affect the outcome of induction heating of carbon fiber composites.

57

5.2 Heating Mechanisms

In the beginning of the 90's, studies were started at two universities, Stanford, and University of Delaware on the heating of carbon fiber reinforced plastics. Both universities came to the same conclusion [30]. The subdivisions they made in induction heating of CFRC's is shown in Figure 5.2.
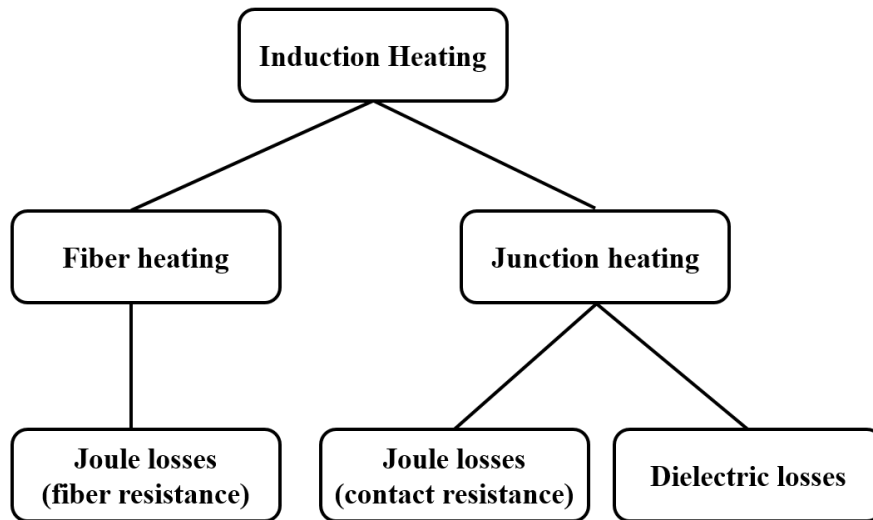
Figure 5.2: Subdivision in heating of CFRC's [5].

There are three possible heating mechanisms. The consolidation of the laminate greatly affects the way the junctions are built. Poor consolidation will cause the fibers to be separated by a region of resin. On the other hand, many fibers will be in contact when the material is consolidated well [30]. Either one of the heating mechanism may take place, or all the three mechanisms can take place at the same time.

5.3 Ansys Maxwell Simulation Models

To examine the parameters that affect the heating on carbon fiber composites many simulations models were developed and performed. The parameters that were varied were

www.manaraa.com

fiber diameter, fiber-to-fiber distance, models with resin, models without resin, fiber orientation, etc. Solid loss values were computed for comparison between the simulation models. As it is well known the computed solid loss would be directly proportional to the heat generated.

5.3.1 Initial Simulation Models

5.3.1.1 Model with Two Layers of Carbon Fiber Oriented in the Same Direction

One simulation model created is shown in Figure 5.3. In this, all parameters were selected randomly. There was no resin material present in the model. The conductive copper coil of length, width, and height of 25 mm, 25 mm, and 5.5 mm, respectively was placed at a distance of 6 mm from the top layer of the carbon fibers. The cross section of the conductor is a rectangle, with the width (w) of 4.5 mm and height (h) of 5.5 mm. Here, the carbon fibers were created using polylines with circular cross-section. As seen in the Figure 5.3, there are two layers of carbon fibers, and all are aligned in the same direction.

The diameter and length of each carbon fiber is 0.2 mm, and 25 mm, respectively. The center-to-center distance between any two fibers in the same layer is 2.7 mm. Moreover, the center-to-center distance between the two layers is 0.4 mm. The conductivity of carbon fibers is assumed to be of 3000 (S/m). The coil is excited using a 500 A AC current at a frequency of 292 KHz.

59
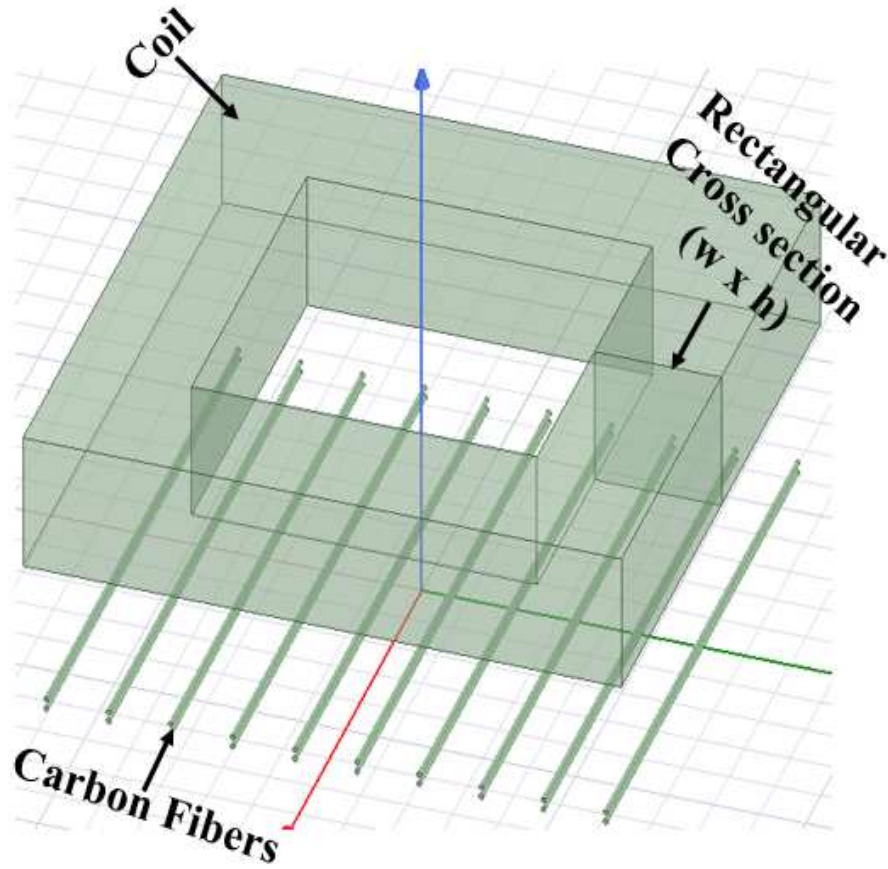
Figure 5.3: Simulation model with two layers of carbon fibers oriented in one direction.

After the simulation was complete computed solid loss obtained was 1.08×10^{-5} **W.** The results obtained is because of Joule heating (fiber resistance). The solid loss value is significantly low because in the simulation model the number of carbon fibers are less compared to millions of fibers in a real carbon fiber ply.

To examine the effect of various parameters on the outcome (solid loss) more models were created. In the new models, the only changes were made was on the carbon fibers. All models with changes are explained in detail one by one.
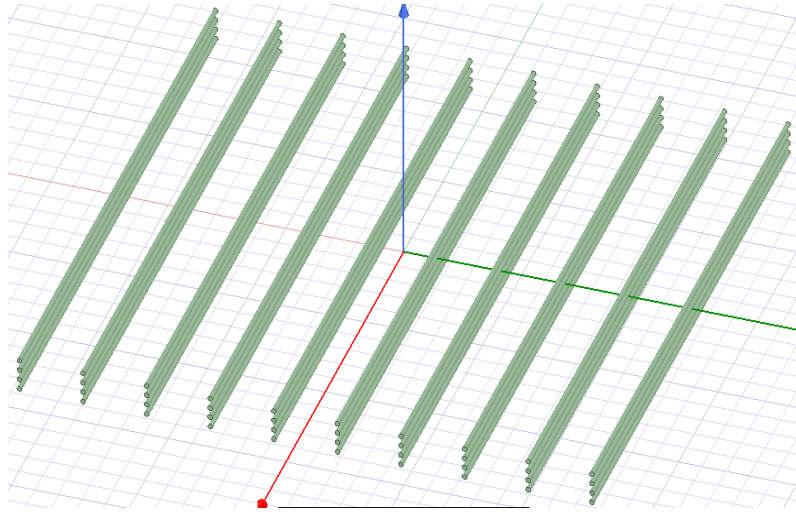
5.3.1.2 Model with Two Layers of Carbon Fibers with 0's and 90's Fiber Orientations
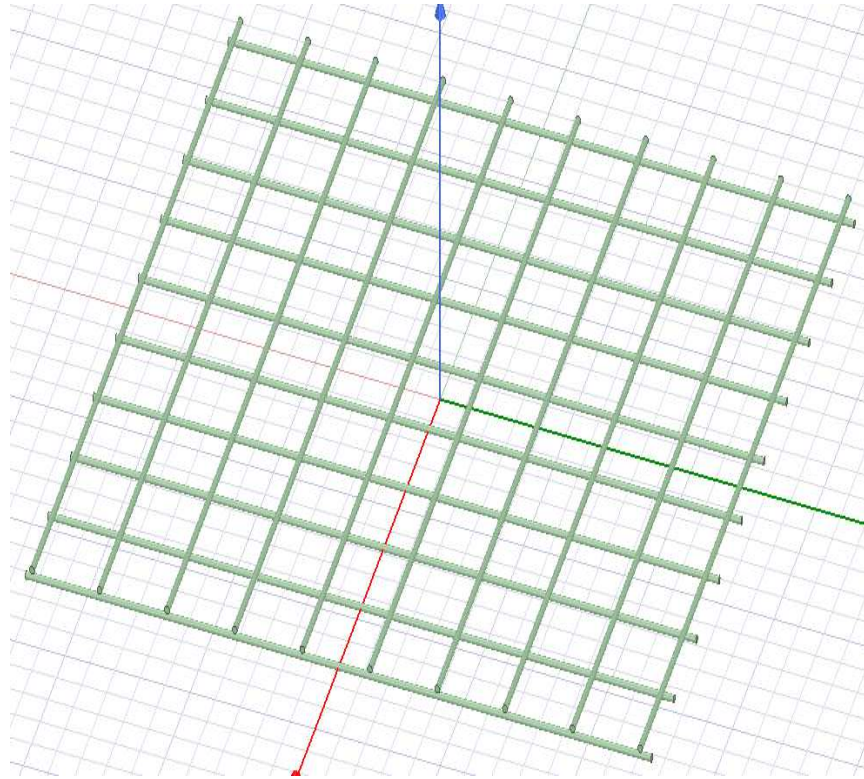
Figure 5.4: Two layers with 0's and 90's fiber orientation.

In this model (see Figure 5.4), the only change made was that here instead of all carbon fibers being in the same direction, fibers in one layer was in the x-direction and the fibers in another layer was in the y-direction. Hence, both the layers were perpendicular to each other (i.e., 0 and 90). The solid loss obtained for this model was 1.92×10^{-5} **W.** The result obtained is due to Joule heating and cross-induced current. Comparing the result with the previous simulation model result, it shows that 0 and 90 fiber orientation setup gives higher solid loss. However, the difference in the values for both the models is not significant the reason could be that there are fewer fibers and there is no resin.

61

5.3.1.3 Model with Four Layers of Carbon Fiber Oriented in the Same Direction

Figure 5.5: Four layers with all fibers oriented in one direction.

In Figure 5.5 there are four layers of carbon fibers where all the fibers are oriented in the same direction. Computed solid loss was 2.02×10^{-5} W. Compare with model1 which has the same case but had half the number of fibers. Looks like the loss just doubled and because of entirely due to the doubling of the numbers of fibers.

5.3.1.4 Model with Four Layers of Carbon Fiber with 0's and 90's Orientations
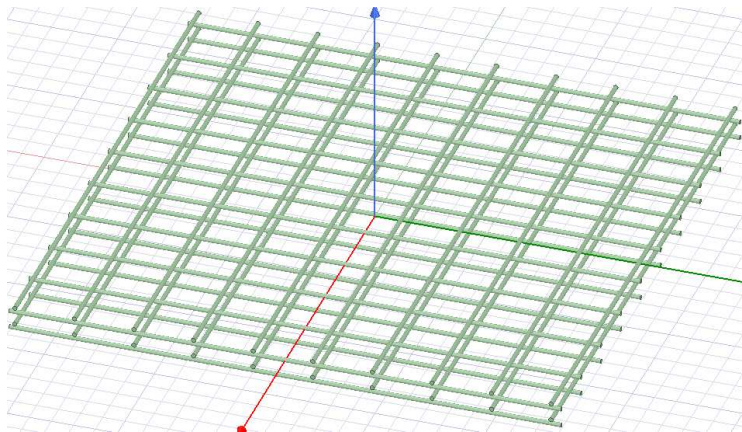
Figure 5.6: Four layers with 0's and 90's orientation.

Figure 5.6 shows the simulation model with four layers of fibers with two layers in 0-degree orientation and two layers in 90-degree orientation. The 0 and 90 orientation arrangement is alternate (i.e. 0 90 0 90). The solid loss obtained for this model is 2.11×10^{-5} **W**. Comparison of results obtained for all four models is shown in Table 5.1.

Table 5.1: Comparison of four models discussed above.

| Simulation Models	Solid Loss (Watts)
[0 0]	1.08e-5
[0 90]	1.92e-5
[0 0 0 0]	2.02e-5
[0 90 0 90]	2.11e-5

As shown in Table 5.1 the solid loss obtained for four layers of simulation model with 0's and 90's fiber orientation is higher compared to other three models. Moreover, the results suggest that if there are more number of fibers, the output results will also increase.

5.3.2.1 Four Layers Simulation Model with More Number of Fibers.

In these simulation models, there are more numbers of carbon fibers for both the models with four layers shown in the previous section. The number of carbon fibers is doubled.

63
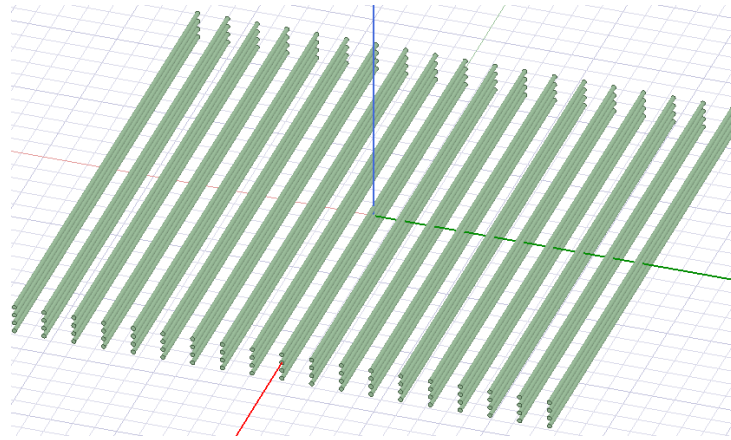
(a)
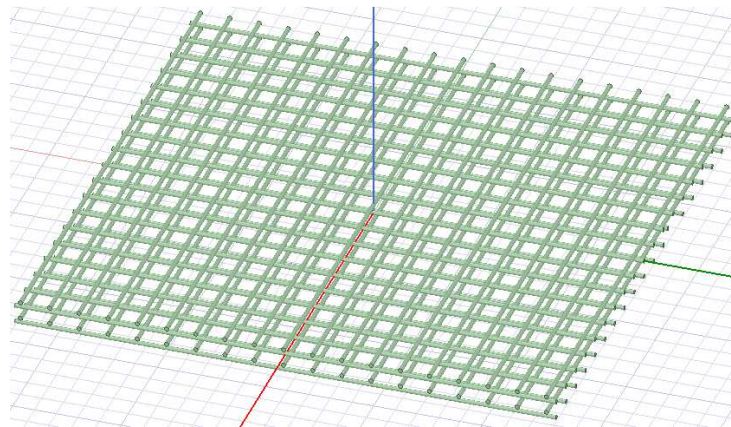
(b)

Figure 5.7: Four layers models with more fibers (a) same orientation, (b) 0 and 90 orientation.

Fig 5.7 represents the simulation models with more number of carbon fibers. One model has all the carbon fibers in the same direction whereas another model has 0 and 90 orientation. The solid loss obtained for all the fibers in the same orientation and 0 and 90 orientation are 3.72×10^{-5} and 3.94×10^{-5} **W,** respectively. These results are comparatively higher compared to that of the previous section. This explains that more carbon fiber gives

64

higher solid loss. Moreover, the results explain that the results for 0 and 90 orientation is higher compared to the fiber orientated in the same direction.

5.4 Hypothesis of Interface Heating

Results obtained for different simulation models until now suggest that heating in a laminate takes place in a very thin area where two plies with different fiber direction meet. Hence, to verify this hypothesis a series of models with two plies were created and simulated. One ply with 0 degrees and the other with 90 degrees fibers orientation. Also, using a fixed coil distance to the welding plane. Adding layers of individual fibers to the two plies as follows:

1. [- - 90] and [0 - -]
2. [- 90 90] and [0 0 -]
3. [90 90 90] and [0 0 0] and so on.

Looking at the ply with a microscope, it was found that there are around 30 layers of individual fibers in one ply. Therefore, the last simulation model will be [30(90)] and [30(0)]. If heat generation is less in the plies with respect to the numbers of fibers, it can be concluded that heating is limited to the fibers close to the interface. If this hypothesis is correct, simulation modeling will be easy because it will be then limited to only a few layers of carbon fibers.

Figure 5.8 represents the first simulation model for the hypothesis. In this model, there are two layers of fibers, 0 and 90 orientation. The fibers are created using cylinders. The diameter and length of the carbon fibers are 0.07 mm and 5 mm respectively, and the distance between two fibers in the same layer is 0.07 mm. In addition, the distance between
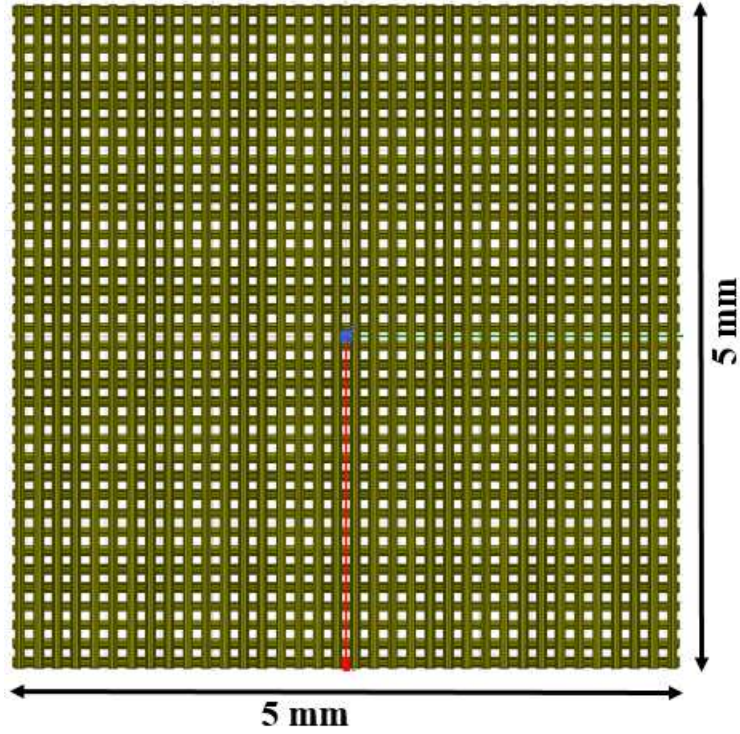
the two layers is 0.07 mm. There is a conductive coil on top of the fibers at 6 mm distance from the plane. The coil has a rectangular cross-section of 1.5 mm x 0.75 mm.
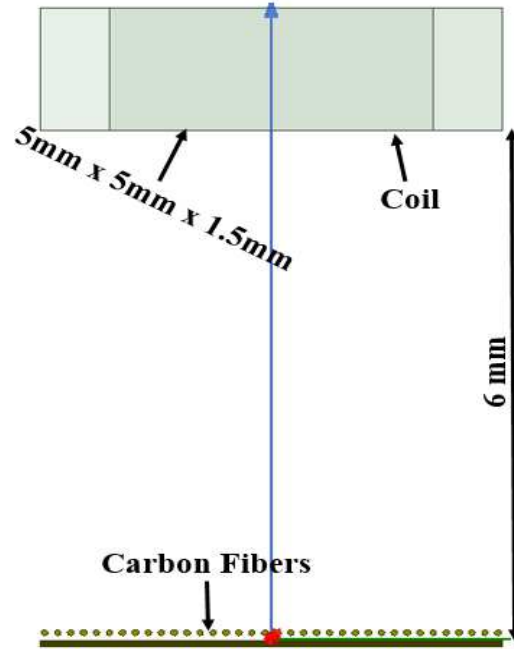
(a)
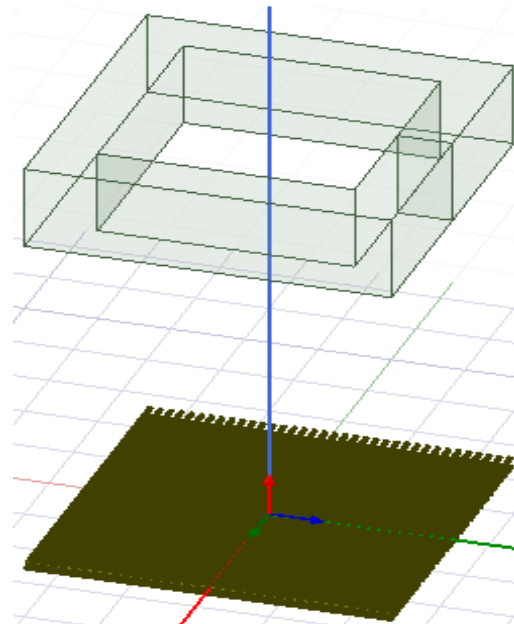
(b)

(c)

Figure 5.8: Hypothesis simulation model (a) side view, (b) trimetric view, (c) top view.

More models were created by adding layers of fibers to the plies as explained before in this section. The results for the first three models are shown in Table 5.2.

Table: 5.2: Comparison of results for three models created using cylindrical shape fibers.

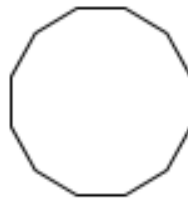| No. of layers	Solid Loss	Tetrahedral	No. of fibers	Status
[- - 90 , 0 - -]	1.1459E-8	1986415	72	Normal
[- 90 90 , 0 0 -]	2.0184E-8	2503686	144	Error
[90 90 90 , 0 0 0]	3.2964E-8	2900326	216	Error

From Table 5.2, simulation for the first model did complete but for other two simulations did not complete because of limited computer memory. With the increase in a number of carbon fibers, the number of tetrahedras also increase. The number of tetrahedras are almost 3 million for the third simulation model. Using the results shown in Table 5.2, nothing can be concluded. The increase in a number of tetrahedras is because of the curved shape of carbon fibers. Therefore, carbon fibers were created using an alternate method to overcome this problem.

5.4.1 Alternative of Cylindrical Fibers

1) **Circle to square:** Using formula, a circle can be represented as a square.

$$A = \frac{Radius}{0.59}$$
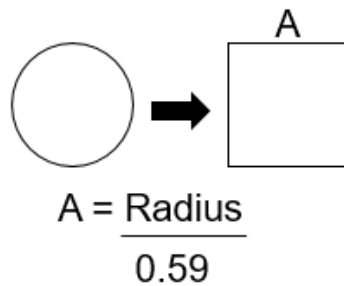
2) **Polyhedron:** Instead of using cylindrical shape, polyhedron shape can be used, which helps in reducing the number of tetrahedras. Because here a circle is created using 12 small line segments as shown below.


Polyhedron

Table: 5.3 shows the comparison for all three different shape carbon fibers simulation results.

Fiber shape	Solid Loss	Tetrahedral	No. of fibers	Status
[90 , 0] Cylinder	1.1459E-8	1986415	72	Normal
[90 0] Square	6.6528E-9	249702	76	Normal
[90 , 0] Polyhedron	8.8997E-9	190708	72	Normal

For all three different shapes consisting of one layer of 0's and one layer of 90's oriented carbon fibers the simulation did complete without error. Polyhedron shape carbon fiber is the best compared to other two simulation models. In addition, the solid loss value of the polyhedron model is very close to that of cylinder shape fibers model. After this comparison, polyhedron shape carbon fiber was used for all the models. The last model for which simulation did complete consisted of 17 layers of 90's and 17 layers of 0's.
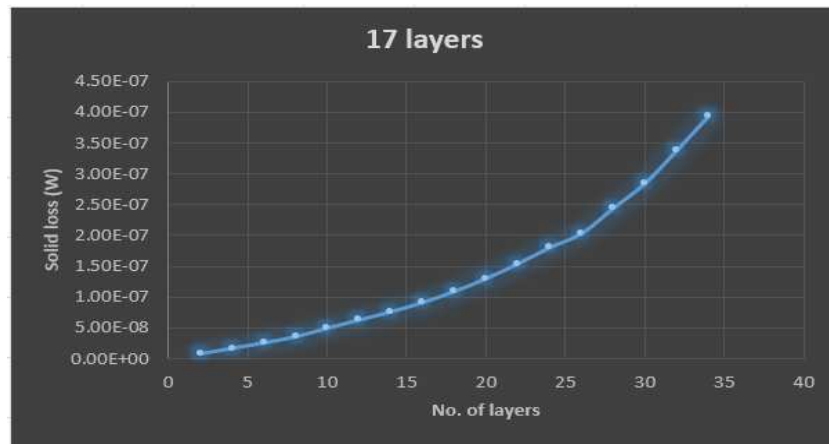
(a)

Figure 5.9: Simulation results (a) obtained results.

Figure 5.9 shows the results obtained from the simulations. The expectation was that after a certain number of carbon fiber layers the solid loss value should stabilize and become monotonics. Because the 0 and 90 intersection layers will be at some distance that they will not interact with each other. However, from the simulation results, it is clear that the hypothesis is not valid. There could be possibly two reasons for the miss-match between simulation results and expected results. The first reason could be that in the simulation model there was no resin in between the layers. The other reason could be that the model was not created using the exact dimensions of real-world carbon fiber plies. Moreover, as the number of layers in each ply increases, the top layer of carbon fiber is getting closer to the coil and therefore the solid loss obtained is getting larger. If the model was made using actual parameters, the results could have been different. This hypothesis was not examine with actual parameters in simulation models because of the limited computer memory.

5.5 Ansys Maxwell Simulation Model Development with Actual Parameters

More simulation models were created to verify the results obtained in section 5.3. The simulation models in this section were created using the parameters of real-world carbon fiber plies. In most of the plies, the ratio of carbon fiber to resin is 65 percent. There is 65 percent of carbon fiber and 35 percent of resin. Using this information fiber-to-fiber distance in the same layer is calculated.

The parameters for new models were used are as shown in Figure 5.10. The diameter of carbon fiber is $7\mu m$ and the surface-to-surface distance between the fibers is $0.7\mu m$.
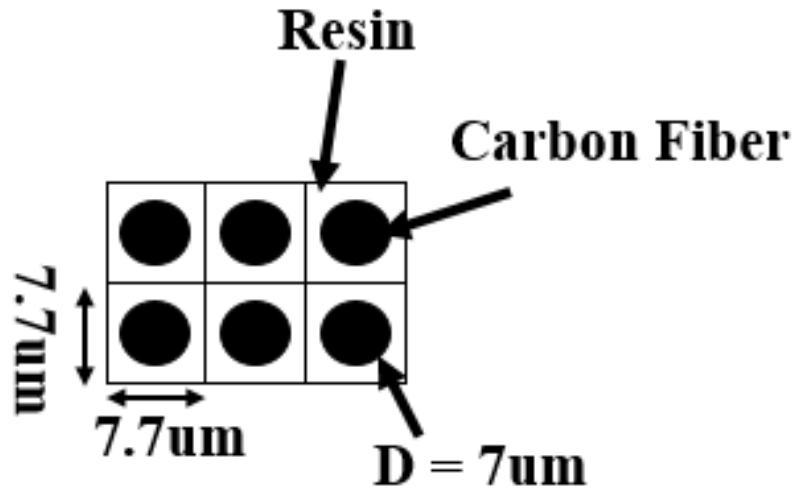
70

Figure 5.10: Parameters for 65 % volume fraction.

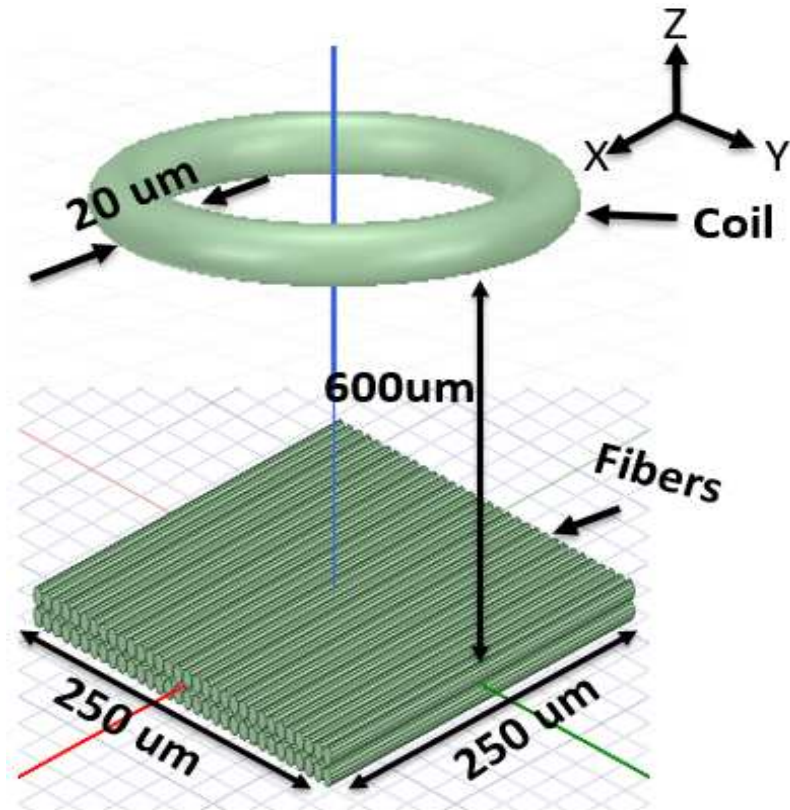**5.5.1 Model with Two Layers of Carbon Fiber in the Same Direction**

Figure 5.11: Simulation model with all fibers in the same direction.

In Figure 5.11, the simulation model has two layers of carbon fibers. Carbon fibers in both layers are oriented in the same direction. The diameter of a fiber is $7\mu m$ and its length is $250\mu m$. The surface-to-surface distance between two fibers in the same layer is $0.7\mu m$ and the distance between two layers is $0.7\mu m$. The coil is made of a copper and is placed at a distance of $600\mu m$ from the center of the two layers. The diameter of the coil is $20\mu m$. There is no resin present in this model. The coil is excited using 500 A AC current at a frequency of 292 KHz. The solid loss obtained for this model is 8.76×10^{-14} W. The result obtained is due to fiber resistance.

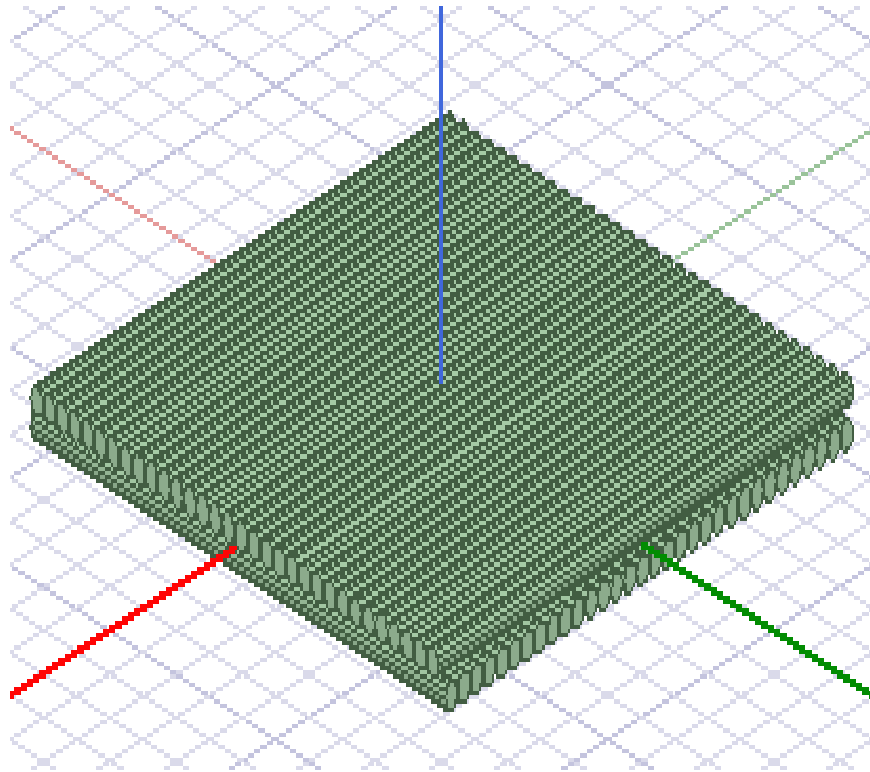**5.5.2 Model with Two Layers of Carbon Fiber with 0's and 90's Fiber Orientations**


Figure 5.12: Two layers with 0's and 90's orientation.

In this simulation model, there are two layers of carbon fibers. One layer of carbon fibers is arranged in 0 orientation and another layer in 90 orientation. The layers are perpendicular to each other. The solid loss obtained for this setup was 8.91×10^{-14} W. The result obtained is due to fiber resistance and cross-induced current. The result is slightly higher compared to the results with all carbon fibers in the same direction.

5.5.3 Simulation Model with Conductive Resin
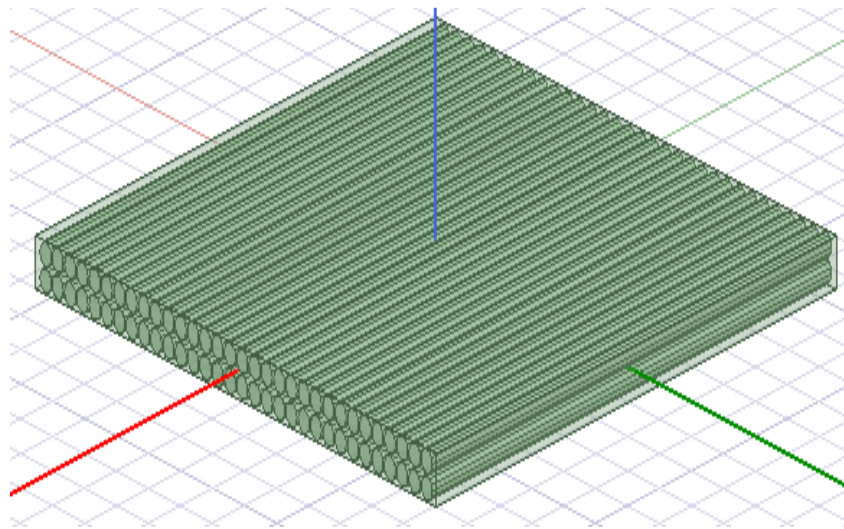
Figure 5.13: All the fibers are oriented in same direction in the presence of conductive resin.

The simulation model is the same as Figure 5.11. The only difference is that in this model there is a conductive resin. In this model, first, the carbon fibers were created. After which, a conductive resin box was created on top of the fibers. Then the carbon fibers were subtracted from the resin box, creating holes in the resin box. Those holes were filled with carbon fibers. Hence, each carbon fiber is covered by conductive resin from all four sides. The average through-the-thickness electric conductivity is in the range of 0.1 to 1.0 (S/m) [6]. The conductivity of resin used in all simulation models was 1.01 (S/m). The solid loss

obtained was 6.4×10^{-13} **Watts**. The result obtained is due to fiber resistance and fiber contact. Here, fibers are in contact because of conductive resin in between the layers. Even though, all of the fibers are in the same direction the result obtained is higher than the model with 0 and 90 orientation without resin. Hence, the role of the conductive resin is significant.

5.5.4 Simulation Model with 0's and 90's Fibers Orientation in the Presence of Conductive Resin.
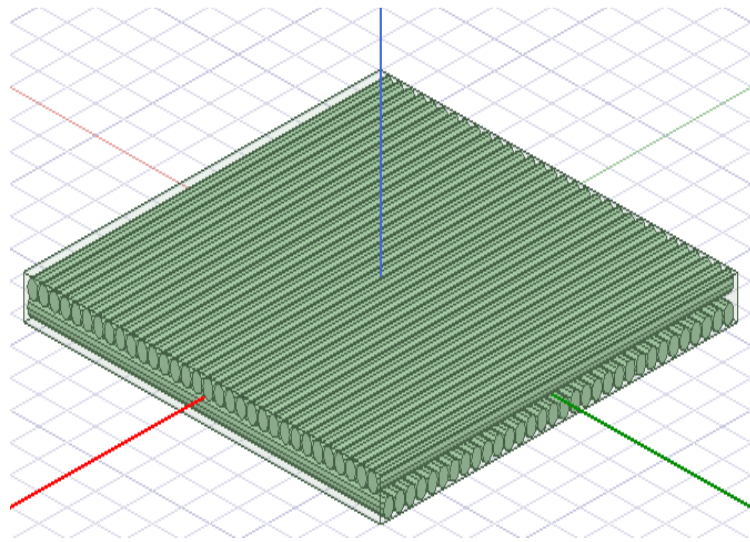
Figure 5.14: Two layers model with 0 and 90 orientation in the presence of conductive resin.

Figure 5.14 represent the model with two layers of carbon fiber oriented as 0 and 90 in the presence of conductive resin. Solid loss obtained is 1.7×10^{-11} **Watts**. The result obtained is due to fiber resistance, cross-induced current and fiber contact. The results obtained for this model is higher compared to all previous models in this section. This explained that the orientation of carbon fibers and the resin are two important parameters to consider. Results for all four models in this section is shown in Table. 5.4

74

Table 5.4: Comparison of results with and without conductive resin.

Simulation Models	Solid Loss (Watts)	Factor
[0 0] no resin	8.76e-14	1
[0 90] no resin	8.91e-14	1.0171
[0 0] with resin	6.40e-13	7.3059
[0 90] with resin	1.70e-11	194.0639

From the comparison, it is clear that the fiber orientation and the resin both plays a vital role in output result. To study the effect of fiber orientation and the resin more simulation models were created which are explained in the following section.

5.6 Study the Effect of Fiber Orientation and the Presence of Resin

In this section, simulation models were created to study the effect of fiber orientation and the presence of resin.

**5.6.1 Effect of Amount of Resin Presence in Between the Fiber Layers.**

Using a microscope, it was found out that the gap between two layers of carbon fiber varies from $0.5 \mu m$ to $24 \mu m$. At some places, the distance between the two layers is less whereas at other

places it is large. To study the effect of the amount of resin present between the fiber layers simulation model was created as shown in Figure 5.15.
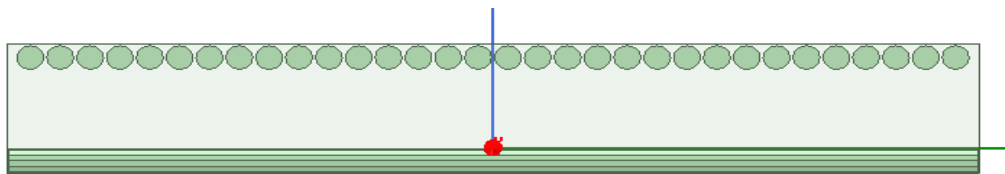
75
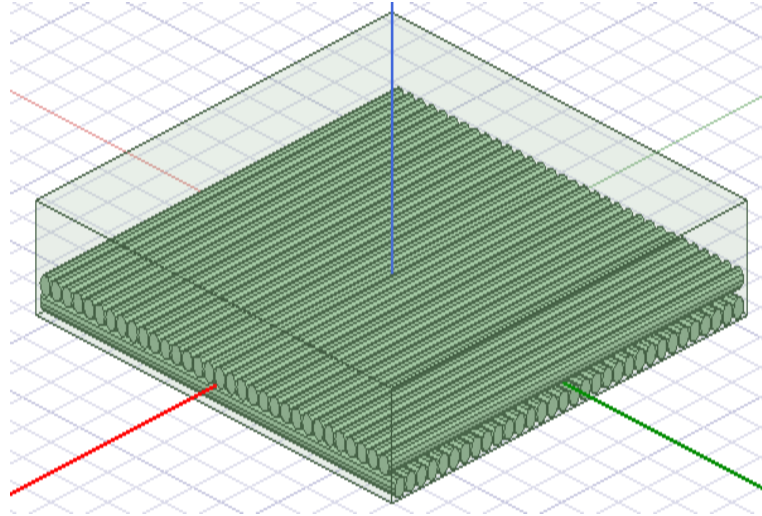
Figure 5.15: Two-layer model with 3-fiber diameter resin on top.

There is a resin rich layer on top of fibers. This layer of resin is approximately 3-fiber diameter. The distance between two fiber layers was varied to study the effect of the amount of resin in between the fiber layers.
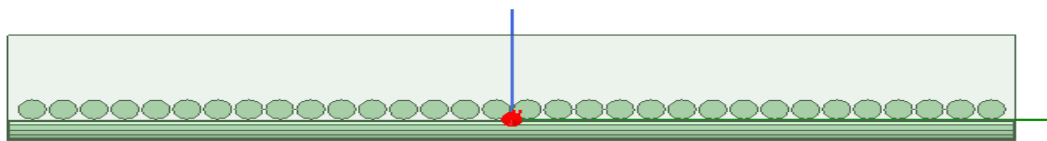

(a)

(b)

Figure 5.16: Simulation models (a) spacing of $0.5 \mu m$ between the layers, (b) spacing of $23.5 \mu m$ between the layers.

As shown in Figure 5.16, simulation with less resin to more resin between the layers were created. Total 47 models were simulated. The first model simulated was with the gap of $0.5\mu m$ between the layers. Next model simulated was with a gap of $1\mu m$. Similarly, more simulation models were created with the step increase of $0.5\mu m$ all the way up to $23.5\mu m$. Simulation for all models did complete and the results obtained are as shown in Figure 5.17.
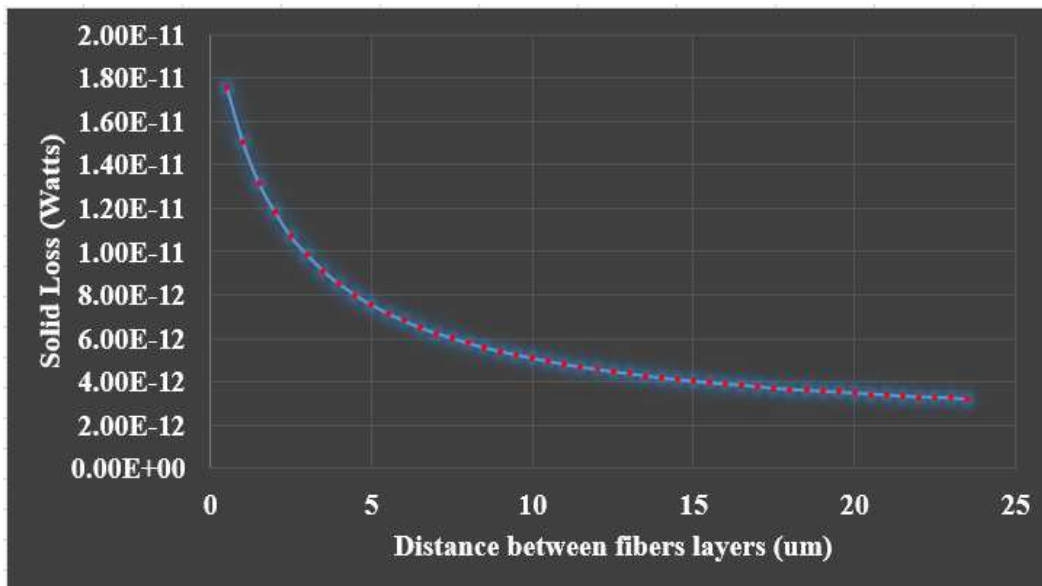

Figure 5.17: Plot of solid loss obtained for all 47 models.

From the plot, it is clear that the simulation model with less resin in between the layers gave higher solid loss. Moreover, as the distance between the layers is increasing (more resin in between) the solid loss obtained is decreasing. There was a sudden decrease in the output results for first few simulation models whereas after a certain distance the decrease in output is constant. This result explains that if there is more resin presence in between the fiber layers, there will be less interaction between the layers hence, there is less intense electric field between the fibers and the output result will be less.

5.6.2 Study the Effect of Fiber Orientation

In the previous section, the effect of resin was examined now in this section effect of carbon fiber orientation will be examined. From previous models in this chapter, it is clear that the 0's and 90's orientation in the presence of resin gives higher output compared to all other simulation models. Simulation models were created using different fiber orientation plies to verify that the 0 and 90 orientation is best among different fiber orientation. Plies with different fiber orientation are shown in Figure 5.18.
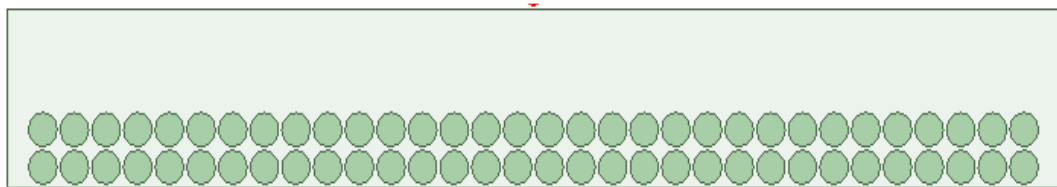
(a)
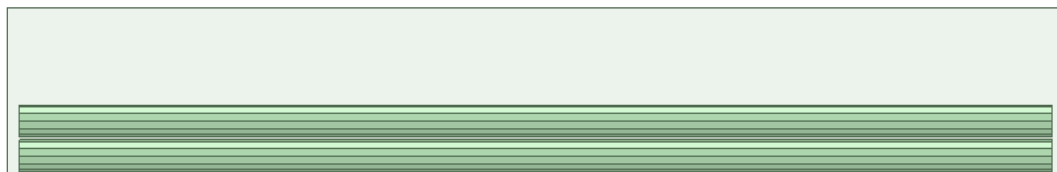
(b)
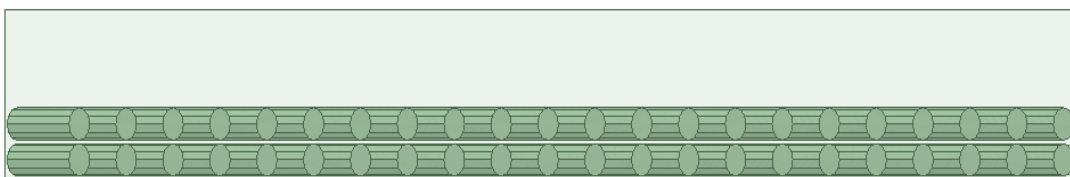
(c)

Figure 5.18: Different fiber orientation plies (a) 0's fibers ply, (b) 90's fibers ply, (c) 45's fibers ply.

78

Figure 5.18 shows different fiber orientation plies with two layers of fibers and resin rich layer of $21\mu m$ on top of the fibers. Using a microscope, it was clear that there are 30 layers of carbon fibers in each ply. In these models, there are only two fiber layers in each ply because the machine on which simulation was performed cannot handle more fiber layers because of limited computer memory.

The three plies are shown in Figure 5.18 were used to create simulation models. Three different combinations of plies and each combination was arranged in three different ways. Total nine simulation models were created using these three plies. All simulation models and their results are as shown below.

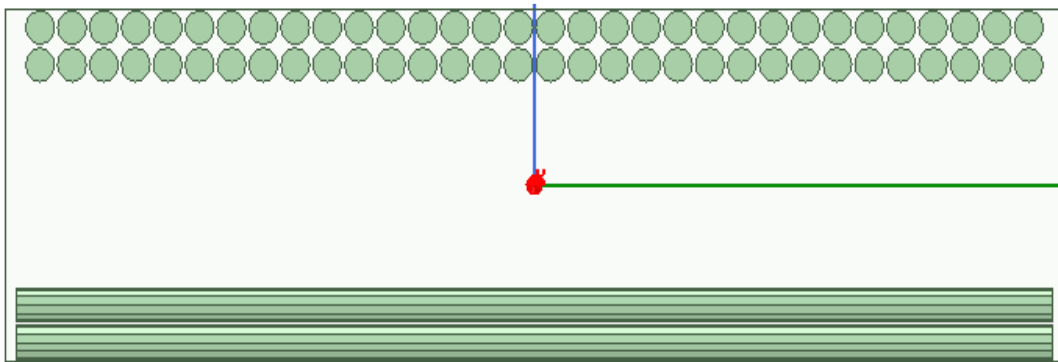**5.6.2.1 Simulation Models with 0's ply and 90's ply**

The first set of simulation was created using plies with 0's fibers and 90's fibers. Both plies were arranged in three different ways to study the effect of fiber orientation and the amount of resin present in between the plies as shown in Figure 5.19.
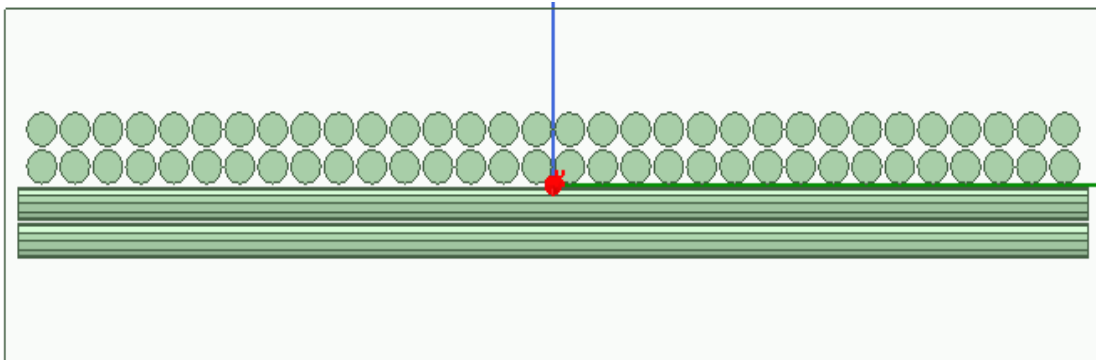
(a)
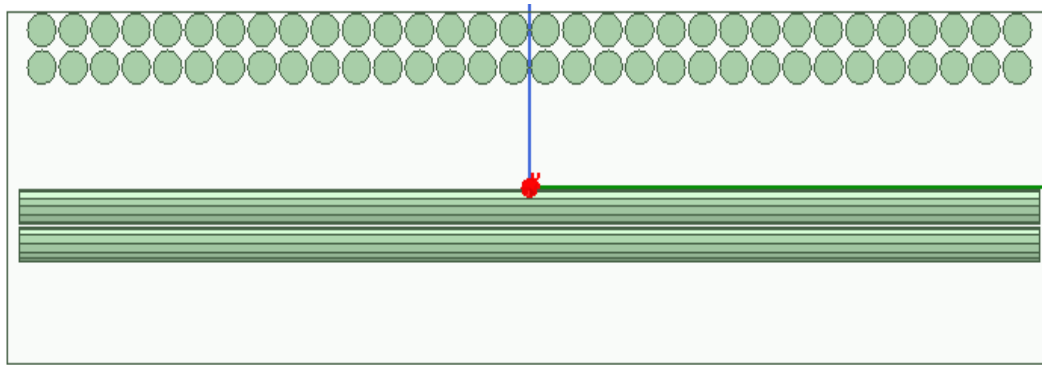
(b)

(c)

Figure 5.19: Three different arrangement with 0's and 90's plies.

Fig 5.19 represent the three simulation models created using 0's and 90's fibers plies. In this simulation models, the arrangement was such that the first simulation has a gap of $0.7\mu m$ between the plies, the second simulation has a gap of $21\mu m$, and the third simulation has a gap of $42\mu m$. Results for these simulations are shown in Table 5.5.

5.6.2.2 Simulation Models with 0's ply and 45's ply

Three simulation models created using the combination of 0's and 45's plies are shown in Figure 5.20.

80
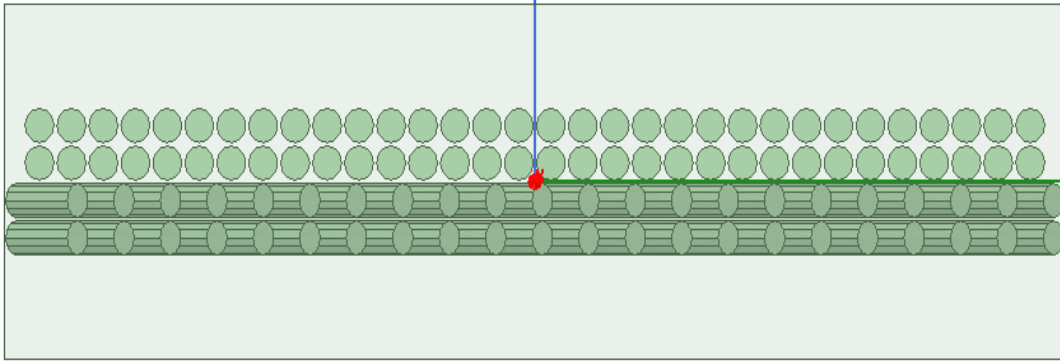
(a)
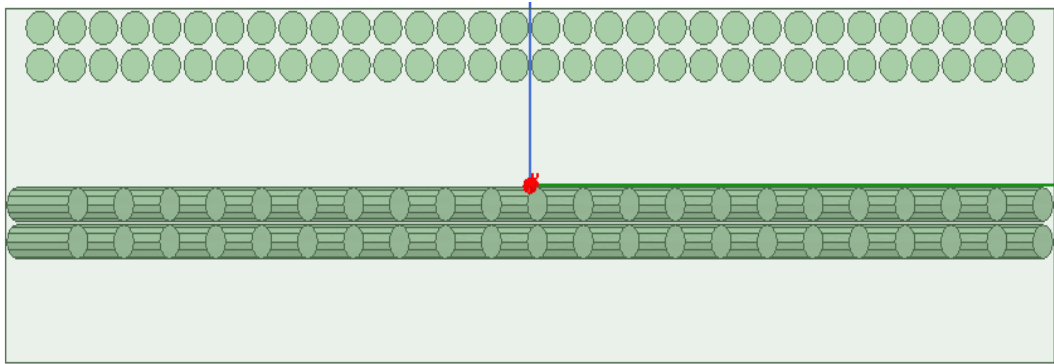
(b)

(c)

Figure 5.20: Three different arrangement with 0's and 45's plies.

The gap between the two plies is the same as the previous three models. Results are shown in Table 5.5.

5.6.2.3 Simulation Models 45's ply and 90's ply

Three simulation models created using the combination of 45's and 90's plies are shown in Figure 5.21.

(a)

(b)

(c)

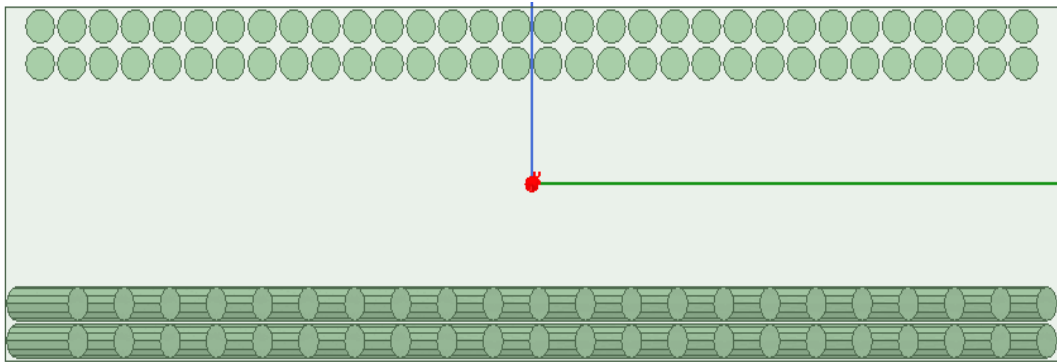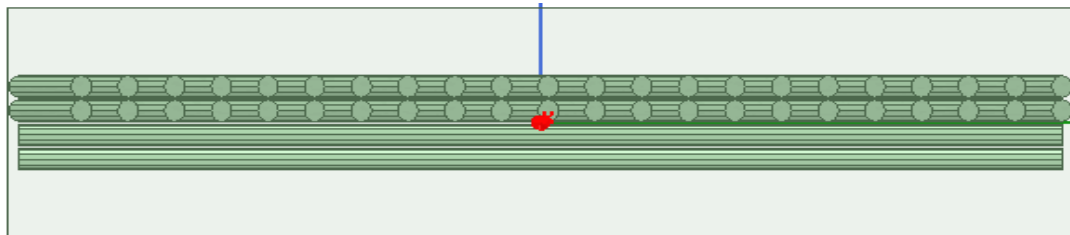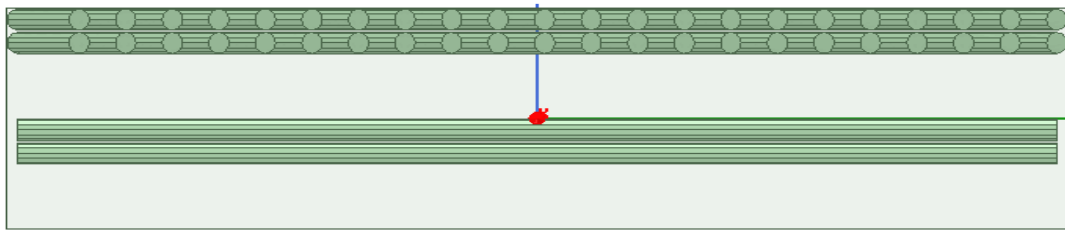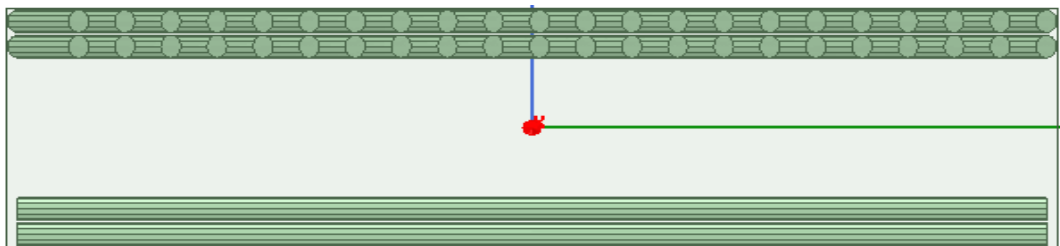**Figure 5.21: Three different arrangement with 45's and 90's plies.**

The gap between the two plies is the same as the previous three models. Results are shown in Table 5.5.

Table 5.5: Results comparison for all nine-simulation models.

Gap Between Plies (μm)	Solid Loss (Watts)		
	0's and 90's plies	0's and 45's plies	45's and 90's plies
0.7	1.99e-11	5.62e-12	5.74e-12
21	4.98e-12	2.72e-12	2.88e-12
42	3.22e-12	2.21e-12	2.37e-12

The comparison shows that the combination of 0's and 90's plies gives the maximum output compared to other combination in all three different gap arrangement. Moreover, as the distance between the plies is increasing the solid loss is decreasing. This explains that if there is more resin in between the fibers, the interaction between the fibers reduces and, in the result, the output is decreased. For all three combinations of plies, the solid loss obtained is higher for $0.7 \mu m$ gap compared to the other two. In addition, for all three gap arrangement 0's and 90's combination gave a higher solid loss.

The parameters that affect the output are carbon fibers orientation and the amount of resin in between the fiber layers. 0's and 90's fiber orientation is better compared to all fibers in the same direction. Moreover, 0's and 90's combination in the presence of resin

gave maximum results compared to all other combinations. The results obtained for all simulation models are very small the reason could be, in simulation models, there are less than a hundred carbon fibers whereas in real ply there are millions of carbon fibers.

CHAPTER 6
CONCLUSION AND FUTURE WORK

6.1 Conclusion

The focus of this thesis was to study induction based thermoplastic welding by performing electromagnetic simulations and analysis. The major topics addressed here include the EM (1) analyses of the welding of two parts of Thermoplastic Composites (TPC) in the presence of a susceptor, (2) the analytical studies of fiber heating due to EM waves, and (3) carbon fiber heating due to EM waves from a coil.

The issue of inductive heating and welding of two pieces of thermoplastic composites in the presence of a susceptor alloy consisting of 67% nickel and 27% copper (called Monel) was studied using Ansys Maxwell. A primary current carrying coil was excited using 500A of current at 292 kHz frequency, which exposed the Monel susceptor underneath it. The EM fields created by the primary coil caused induced currents in the Monel mesh, which caused losses. Temperature rise in the material is synonymous to the losses in the material. The I^2R losses in the Monel material was used as the basis to calculate the temperature rise in the material. Simulation results clearly showed solid losses in the material, which can be used to heat and weld the composite panels. Location based temperature increase due to I^2R losses were calculated which showed significant heating and welding potentials. Simulation and experimental results of temperature increase were compared showing similar outcomes. Measured temperature increase showed the reading

of 40 and 43.9 degrees respectively (thermocouple and IR camera). These numbers compare favorably with the simulated temperature increase of 38.97 degrees C.

Analytical studies of fiber heating due to induction was studied by deriving field equations using the Biot Savart's law. Field values calculated using analytical method were compared from field values computed using Maxwell. In general, the results from the two methods were close. Differences occurred due to the geometry differences in the primary source and the effect of the diameter of the coil in the simulation model, which did not exist in the analytical method.

Finally, the induction heating of Carbon fiber reinforced composites (CFRC) were simulated and studied. The results obtained from the simulation explain that fiber orientation and the presence of resin are two critical parameters that affect the output e.g. the solid loss. Due to the challenges in the high aspect ratio of the models, i.e. very small fiber diameters and many fibers within a very small dimension only smaller sized models were simulated. Furthermore, instead of a circular cross-section a polyhedron cross-section for the fiber model was considered to successfully complete the simulations. It was found that simulation models containing fibers oriented in 0 and 90 orientation yielded for solid loss than fibers oriented in the same direction. It was observed that for fibers with resin present in between them yielded far greater solid loss compared to no-resin cases, especially for very small separation distances between fibers. Especially, for the 0, 90 orientation of fibers and in the presence of resins solid loss was nearly 200 times that for fibers with 0,0 orientation and that were at short distance from one another.

6.2 Future Work

Future work should include the development of simulation models that can consider larger specimens and multiturn coils. Fiber to fiber contact should also be considered. Some form of macroscopic simple models that could be circuit based could be developed which will alleviate the challenges of large scale full-wave simulations using Finite Element Methods. Other forms of dielectric materials could be considered along with joining parts that are at angles.

REFERENCES:

[1] The Balance Careers. (2018). *Advantages and Disadvantages of Composite Materials on Airplanes*. [Online] Available at: https://www.thebalancecareers.com/composite-materials-aircraft-structure-282777.

[2] Wikipedia. (2018). *Thermoplastic*. [Online] Available at: https://simple.wikipedia.org/wiki/Thermoplastic.

[3] En.wikipedia.org. (2018). *Thermoplastic*. [Online] Available at: https://en.wikipedia.org/wiki/Thermoplastic.

[4] Ageorges, C., Ye, L., 2001, "Simulation of impulse resistance welding for thermoplastic matrix composites", Applied Composite Materials, Vol. 8, No.2, pp. 133-147.

[5] Ageorges, C. et al., 2000, "Experimental investigation of the resistance welding for thermoplastic-matrix composites. Part I: heating element and heat transfer", Composites Science and Technology, Vol. 60, No.7, pp. 1027-1039.

[6] Yousefpour, A. et al., 2004. "Fusion bonding/welding of thermoplastics composites", Journal of thermoplastic Composite Materials, Vol.17, No.4, pp. 303-341.

[7] J. Aerosp. Technol. Manag., Sao Jose dos Campos, Vol.4, No 3, pp. 255-265, Jul.-Sep., 2012.

[8] Kagan, V. and Nichols, R.J., 2005, "Benefits of induction welding of reinforced thermoplastics in high performance applications", Journal of Reinforced Plastics and Composites, Vol. 24, No.13, pp. 1345-1352.

[9] Stavrov, D. et al., 2003, "Experimental investigation of large-scale welding of carbon fiber thermoplastic composite materials", In: Proceedings of ICCM -14 Conference, 2003, San Diego.

[10] Yang, F. and Pitchumani, R., 2002a, "Healing of thermoplastics polymers at an interface under nonisothermal conditions", Macromolecules, Vol. 35, No.8.

[11] Yang, F. and Pitchumani, R., 2002b, "Interlaminar contact development during thermoplastic fusion bonding", Polymer Engineering & Science., Vol. 42, No.2.

[12] Xiao, X.R. et al., 1992, "Processing and modelling of resistance welding of ACP-2 composites", Journal of Composite Materials, Vol. 26, No. 7.

[13] Balle, F. et al., 2009, "Ultrasonic metal welding of aluminum sheets to carbon fiber reinforced thermoplastic composites", Advance Engineering Materials, Vol. 11, No. 1.

[14] Wang, X. et al., 2006, "FEM investigation of the temperature field of energy director during ultrasonic welding of PEEK composites", Journal of Thermoplastic Composite Materials, Vol. 19, No. 5.

[15] Kruger, S. et al., 2004, "Ultrasonic welding of metal joints", Advance Engineering Materials, Vol. 6, No. 3.

[16] Levy, A. et al., 2008, "Ultrasonic welding of thermoplastic composites: modelling of the process", International Journal of Material Forming, Vol. 9, No. 1.

[17] Siddiq, A. and Ghassemieh, E., 2008, "Thermomechanical analyses of ultrasonic welding process using thermal and acoustic softening effects", Mechanics of materials, Vol. 40, No. 12.

[18] I. Newman, "Product focus - MONEL alloy 400", *Corrotherm.co.uk*, 2018. [Online]. Available: https://www.corrotherm.co.uk/blog/product-focus-monel-alloy400.

[19] *Magellanmetals.com*, 2018. [Online]. Available: https://www.magellanmetals.com/tube-montel-400.

[20] T.J. Ahmed, D. Stavrov, H.E.N. Bersee, A. Beukers, 2005, "Induction welding of thermoplastic composites-an overview."

[21] Von Margot Gayle; David W. Look; John G. Waite (1992). "Monel *Metals in America's historic buildings: uses and preservation treatments.* DIANE Publishing. pp. 39-41

[22] "MONEL 400 Alloy (UNS N04400)", *AZoM.com*, 2018. [Online]. Available: https://www.azom.com/article.aspx?ArticleID=9338.

[23] "Monel | alloy", *Encyclopedia Britannica*, 2018. [Online]. Available: https://www.britannica.com/technology/Monel.

[24] "Monel 400: Properties and Composition", *The Balance*, 2018. [Online]. Available: https://www.thebalance.com/monel-400-properties-and-composition-2340256.

[25] "Monel", *En.wikipedia.org*, 2018. [Online]. Available: https://en.wikipedia.org/wiki/Monel#cite_note-2.

[26] Chu, H. C., S. K. Jeng, and C. H. Chen, "Reflection and transmission characteristics of lossy periodic composite structures," IEEE Trans. Antennas Propag., Vol. 44, No. 3, 580–587, 1996.

[27] *Protechcomposites.com*, 2018. [Online]. Available: http://www.protechcomposites.com/content/CarbonFiberBasicsWhitePaper.pdf.

[28] Evans, R. W., "Design guidelines for shielding e ectiveness, current carrying capability, and the enhancement of conductivity of composite materials," NASA Contractor Report, No. 4784, 1997.

[29] "Carbon fiber reinforced polymer", *En.wikipedia.org*, 2018. [Online]. Available: https://en.wikipedia.org/wiki/Carbon_fiber_reinforced_polymer.

[30] M. van Roermund, 2007, "Induction heating of carbon laminates," KVE Composites Group.

[31] "File:Composite 3d.png - Wikimedia Commons", *Commons.wikimedia.org*, 2018. [Online]. Available: https://commons.wikimedia.org/wiki/File:Composite_3d.png.

[32] "Composite material", *En.wikipedia.org*, 2018. [Online]. Available: https://en.wikipedia.org/wiki/Composite_material.